An unexpected role for the conserved ADAM-family metalloprotease ADM-2 in *Caenorhabditis elegans* molting

Braveen B. Joseph, Sarina M. Bernazzani, Phil T. Edeen, Shaonil Binti, and David S. Fay*

Department of Molecular Biology, College of Agriculture and Natural Resources, University of Wyoming, Laramie, WY 82071

*Corresponding author

Abstract (294/300)

Molting is a widespread developmental process in which the external extracellular matrix (ECM), the cuticle, is remodeled to allow for organismal growth and environmental adaptation. Studies in the nematode *Caenorhabditis elegans* have identified a diverse set of molting-associated factors including signaling molecules, intracellular trafficking regulators, ECM components, and ECM-modifying enzymes such as matrix metalloproteases. *C. elegans* NEKL-2 and NEKL-3, two conserved members of the NEK family of protein kinases, are essential for molting and promote the endocytosis of environmental steroid-hormone precursors by the epidermis. Steroids in turn drive the cyclic induction of many genes required for molting. Here we report a novel role for the sole *C. elegans* ADAM–meltrin metalloprotease family member, ADM-2, as a negative regulator of molting. Whereas loss of *adm-2* led to strong suppression of molting defects in partial loss-of-function *nekl* mutants, overexpression of ADM-2 induced molting defects in wild-type animals. CRISPR genome editing implicated the Zn-binding motif within the metalloprotease domain as critical for mediating the effects of ADM-2 on molting. ADM-2 is expressed in the epidermis, and its trafficking through the endo-lysosomal network was disrupted after NEKL depletion. We also identified the epidermally expressed low-density lipoprotein receptor–related protein, LRP-1, as a candidate target of ADM-2 regulation. Whereas loss of ADM-2 activity led to the upregulation of LRP-1, ADM-2 overexpression caused a reduction in LRP-1 abundance, suggesting that ADM-2 may function as a sheddase for LRP-1. We propose that loss of *adm-2* suppresses molting defects in *nekl* mutants by eliminating a negative regulator of LRP-1, thereby compensating for defects in the efficiency of LRP-1 and sterol uptake. Our findings emphasize the importance of endocytic trafficking for both the internalization of factors that promote molting and the removal of proteins that would otherwise be deleterious to the molting process.

Author Summary (146/150)

The molecular and cellular features of molting in nematodes share many similarities with cellular and developmental processes that occur in mammals. This includes the degradation and reorganization of extracellular matrix materials that surround cells, as well as the intracellular machineries that allow cells to communicate and sample their environments. In the current study, we found an unexpected function for a conserved protein that degrades proteins on the external surface of cells. Rather than promoting molting through extracellular matrix reorganization, the ADM-2 protease can inhibit the molting process. This observation can be explained by data showing that ADM-2 negatively regulates LRP-1, a membrane protein that promotes molting by facilitating the uptake of molecular building blocks at the cell surface that are needed for molting-related signaling. Our data provide insights into the mechanisms controlling molting and link several conserved proteins to show how they function together during development.

65 **Introduction**

66 The cuticle of *Caenorhabditis elegans* is an external extracellular matrix (ECM) required
67 for locomotion, body shape maintenance, and protection from the environment [1, 2]. During
68 larval development *C. elegans* undergoes four molts, a specialized form of apical ECM
69 remodeling, whereby a new cuticle is synthesized under the old cuticle, which is partially
70 degraded and shed [1, 2]. *C. elegans* molting cycles are orchestrated by conserved steroid-
71 hormone receptors, including NHR-23 (an ortholog of human RORC) and NHR-25 (an ortholog
72 of human NR5A1), which collectively control the oscillation of hundreds of mRNAs [2-4]. The
73 production of molting-specific steroid-hormone ligands is thought to be dependent in part on
74 the uptake of environmental sterols by epidermally expressed LRP-1 (the homolog of human
75 LRP2/megalin), a member of the low-density lipoprotein receptor–related protein family [5, 6].
76 Consistent with this, internalization of LRP-1 by clathrin-mediated endocytosis (CME) is
77 essential for normal molting [2, 5-7].

78 We have previously shown that the *C. elegans* protein kinases NEKL-2 (an ortholog of
79 human NEK8/9) and NEKL-3 (an ortholog of human NEK6/7) promote endocytosis of LRP-1 at
80 the apical epidermal plasma membrane. Correspondingly, loss of either NEKL-2 or NEKL-3
81 function leads to a reduction or delay in the expression of molting genes, a failure to complete
82 molting, and larval arrest [2, 8-12]. NEKL-2 and NEKL-3 (NEKLs) are members of the NIMA-
83 related kinase (NEK) protein family, mammalian orthologs of which have been studied primarily
84 in the context of cell cycle regulation and ciliogenesis [13-28]. *C. elegans* NEKLs bind to and co-
85 localize with several conserved ankyrin-repeat proteins, MLT-2 (an ortholog of human ANKS6),
86 MLT-3 (an ortholog of human ANKS3), and MLT-4 (an ortholog of human INVS), referred to here
87 collectively as MLTs, which are essential for the proper localization of NEKLs [9].
88 Correspondingly, loss of MLT functions leads to molting defects that are identical to those
89 observed with loss of the NEKLs [9]. NEKLs and MLTs form two distinct complexes (NEKL-2–
90 MLT-2–MLT-4 and NEKL-3–MLT-3) and are expressed in a punctate pattern in the large
91 epidermal syncytium known as hyp7, in which they are specifically required [2, 8, 9].

92 The cellular and physiological mechanisms by which NEKLs–MLTs impact the molting
93 process through intracellular trafficking have yet to be fully explored. It is likely that NEKLs are

94 required for the uptake and processing of membrane cargo, including LRP-1, that is required for
95 molting. Using a forward-genetics suppressor approach [29], we previously found that loss of
96 AP2 clathrin-adapter subunits, as well as the AP2 allosteric activator FCHO-1 can suppress
97 molting and trafficking defects in NEKL mutants [11]. These and other studies revealed that
98 NEKLs control endocytosis in part by facilitating the uncoating of sub-apical clathrin-coated
99 vesicles and may affect additional trafficking processes through the regulation of actin via the
100 CDC-42–SID-3 (corresponding to the human CDC42–ACK1/2) pathway [10, 11].
101 Here we report suppression of *nekl* molting defects caused by loss of the conserved
102 ADM-2 transmembrane metalloprotease. Curiously, although proteases have previously been
103 implicated as positive regulators of molting, we find that ADM-2 exerts a negative influence on
104 the molting process. ADM-2 belongs to the ADAM (a disintegrin and metalloprotease) family of
105 metallopeptidases, which are members of the zinc protease superfamily [30, 31]. ADM-2 is the
106 sole member of the meltrin metalloprotease subfamily in *C. elegans* [32, 33], which in humans
107 consists of ADAM9 (Meltrin γ), ADAM12 (Meltrin α), ADAM19 (Meltrin β), and ADAM33 [34,
108 35]. Notably, knockouts of meltrin family members in mammals have generally not provided
109 clear insights into the roles of meltrins in vivo during development, which may in part be due to
110 genetic redundancies [32, 36, 37]. Here we show that, unlike AP2 and *fcho-1* mutants, loss of
111 ADM-2 function did not suppress *nekl*-associated trafficking defects. Rather, ADM-2 was itself
112 dependent on NEKL–MLTs for its uptake and endocytic processing from the epidermal surface
113 where it may act as a negative regulator of LRP-1. Our findings further suggest that loss of
114 ADM-2 may specifically bypass trafficking defects in weak loss-of-function *nekl* mutants by de-
115 repressing LRP-1. Thus, NEKLs may be required for both the internalization of positive and
116 negative regulators of the molting cycle.
117
118 **Results**
119 ***nekl* molting defects are suppressed by reduced function of the ADM-2 metalloprotease**
120 We previously described an approach to identify genetic suppressors of partial loss-of-function
121 mutations in NEKL kinases [29]. Whereas strains homozygous for either *nekl-2(fd81)* or *nekl-*
122 *3(gk894345)* weak loss-of-function alleles are viable, *nekl-2(fd81)*; *nekl-3(gk894345)* double

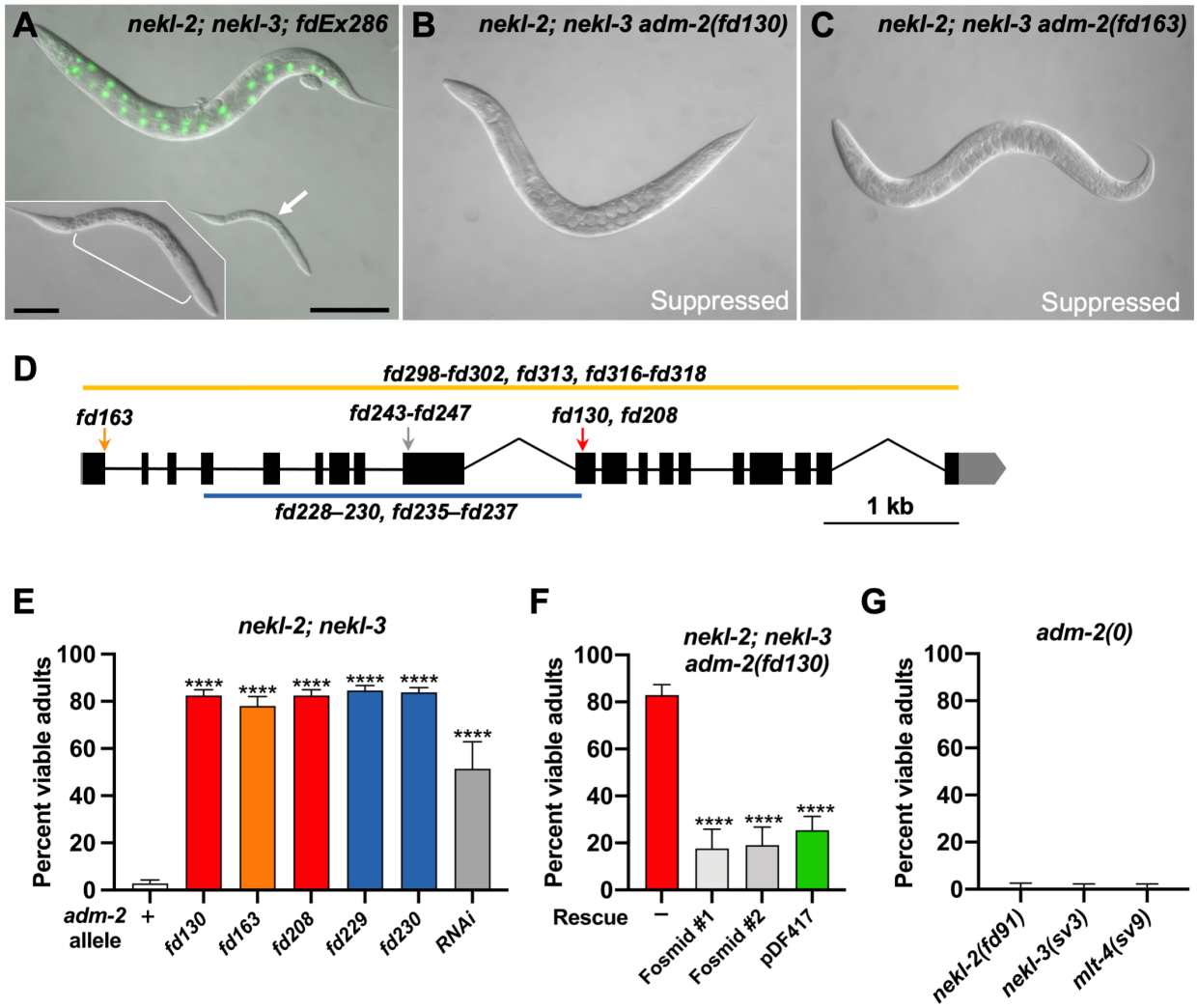

Fig 1. Loss of ADM-2 function suppresses *nekl* molting defects
(A) DIC image of *nekl-2; nekl-3* double-mutant worms. The adult worm contains a rescuing extrachromosomal array *(nekl-3⁺; sur-5::GFP)*. An arrested larva is marked by the white arrow and enlarged in the inset; the white bracket indicates the constricted region containing a double cuticle. (B, C) DIC images of *nekl-2; nekl-3* double-mutant adult worms containing the *adm-2(fd130)* (B) and *adm-2(fd163)* (C) mutant alleles. Bar size in A = 100 μm (for A–C); in inset, 20 μm. (D) Schematic diagram of the *adm-2* locus. Solid black rectangles indicate exons; introns are demarcated by black lines. Locations of the *fd163*, *fd130*, *fd208*, and *fd243–fd247* alleles are indicated by arrows. Large deletion alleles *fd298–fd302 fd313, fd316–fd318, fd228–fd230*, and *fd235–fd237* are indicated by orange and blue lines. (E) Bar plot showing percentage of viable adult-stage *nekl-2; nekl-3* worms with the indicated *adm-2* alleles (or RNAi); + indicates wild-type *adm-2*. (F) Bar plot showing reversion of suppression in *nekl-2; nekl-3 adm-2(fd130)* mutants by fosmids expressing wild-type *adm-2* and by an *adm-2* cDNA fused to GFP (pDF417). Fosmid #1 and #2 indicate two independent extrachromosomal lines. (G) Bar plot showing failure to suppress molting defects in *nekl–mlt* hypomorphic mutants by *adm-2* null mutants [*nekl-2(fd91); adm-2(fd313)*, *nekl-3(sv3); adm-2(fd316)*, and *mlt-4(sv9); adm-2(fd317)*]. Error bars in E–G represent 95% confidence intervals. p-Values were determined using Fisher's exact test; ****$p \leq 0.0001$.

123 mutants (hereafter referred to as *nekl-2; nekl-3* mutants) are synthetically lethal and exhibit
124 ~98.5% larval arrest due to L2/L3 molting defects [9]. In the absence of a suppressor mutation,
125 propagation of *nekl-2; nekl-3* mutants requires the presence of a GFP-marked *nekl-2⁺* or *nekl-3⁺*
126 transgenic rescuing array (Fig 1A and 1E). In contrast, strains homozygous for the suppressor

127 alleles *fd130* or *fd163* of are ~80% viable and propagate in the absence of a rescuing array (Fig
128 1B, 1C, and 1E).
129
130 Using our protocols for whole-genome sequencing and bioinformatical analysis [29], we
131 identified the causal mutation corresponding to *fd130* to be a G-to-A transition in exon 10 of
132 *adm-2*/C04A11.4 (Fig 1D). *fd130* converts codon 494 (TGG; W) into a premature translational
133 termination signal (TGA; stop codon), resulting in the predicted truncation of the 952-amino-
134 acid protein. Correspondingly, the independently isolated allele *fd163* is a G-to-A transition in
135 the conserved 5' splice donor sequence in the first intron of *adm-2* (GT to AT) (Fig 1D). The
136 *fd163* mutation is predicted to result in a stop codon immediately following R66. Using
137 CRISPR/Cas9 methods we isolated several additional *adm-2* alleles including *fd208*, a 1-bp
138 deletion that causes a frameshift after Y479, along with *fd229* and *fd230*, deletions that span
139 exons 4–10 and that result in frame shifts after S123 and T122, respectively (Fig 1D). Like *fd130*
140 and *fd163*, these alleles led to similarly robust suppression of molting defects in the *nekl-2;*
141 *nekl-3* background and are predicted to result in strong or complete loss of ADM-2 function (Fig
142 1E).
143
144 Several additional pieces of evidence indicate that it is loss of ADM-2 function that leads to
145 suppression of *nekl-2; nekl-3* molting defects. (1) *adm-2* mutations that suppress these molting
146 defects (e.g., *fd130* and *fd163*) are fully recessive (see Materials and Methods). (2)
147 Extrachromosomal expression of a fosmid clone containing wild-type genomic ADM-2
148 sequences strongly reversed suppression in *nekl-2; nekl-3 adm-2* mutants (Fig 1F). (3) RNAi of
149 *adm-2* led to significant suppression of molting defects in *nekl-2; nekl-3* mutants (Fig 1E). We
150 note that loss of *adm-2* in wild-type backgrounds, including a strong loss-of-function deletion
151 allele, *fd300*, did not appear to impair development, health, or fecundity, indicating that *adm-2*
152 is a non-essential gene (S1A Fig). Consistent with this, no phenotypes have been previously
153 ascribed to *adm-2* mutations.
154

155 ADM-2 is a member of the ADAM (a disintegrin and metalloprotease) family of
156 metallopeptidases, with its closest human homologs belonging to the meltrin subfamily
157 (ADAM9/12/19/33) (S1C Fig) [32, 34, 35]. Meltrins are notable for having functional proteases
158 that contain a histidine-coordinated zinc-binding site, which is also found in ADM-2 (S2 Fig). Like
159 other meltrins, ADM-2 contains an N-terminal cysteine switch, cysteine loop, and disintegrin
160 domain; a transmembrane domain; and several predicted SH3-binding sites in its cytoplasmic C
161 terminus (S2 Fig) [31, 38]. Although linked to a range of human diseases, individual loss-of-
162 function mutations in mouse meltrins have generally not produced robust developmental
163 defects, and no phenotypes have been associated with either of the two *Drosophila* meltrin
164 family members [32, 36, 37].
165
166 We note that WormBase annotates two *adm-2* isoforms that are identical through exon 18
167 (corresponding to aa A915) but differ at the 5' ends of their 19th (terminal) exons; *adm-2a* and
168 *adm-2b* are predicted to encode 952 and 929 aa proteins, respectively. The noncanonical 18th
169 intron acceptor site of *adm-2b* (5-'GCAAAAG-3') occurs 7 bp upstream of the corresponding
170 acceptor site of *adm-2a* (5'-ATTTCAG-3') and terminates translation 76 bp upstream of the stop
171 codon of *adm-2a*. The peptide regions corresponding to exon 19 of *adm-2a* (37 aa) and *adm-2b*
172 (14 aa) do not contain any known domains nor were homologies detected with other proteins.
173
174 To determine if other *C. elegans* ADAM family members may also contribute to molting control,
175 we tested ten other family members for their ability to suppress *nekl-2; nekl-3* molting defects
176 (S1B Fig). We failed to detect suppression after inhibition of each gene using RNAi (dsRNA)
177 injection methods, which were effective in promoting suppression when targeting *adm-2*. Thus,
178 the suppression of *nekl*-associated molting defects by *adm-2* is unique among the *C. elegans*
179 ADAM family members.
180
181 **Suppression by ADM-2 occurs via a mechanism that is distinct from trafficking suppressors**
182 Loss of AP2 clathrin-adapter subunits and loss of the AP2 activator FCHO-1 individually suppress
183 strong and/or null mutations in NEKLs and MLTs through their effects on CME [11]. We

184 therefore tested if an *adm-2* null mutation could also suppress strong loss-of-function alleles of
185 *nekls* and *mlts*. Notably, loss of *adm-2* was unable to restore viability to *nekl-2(fd91)*, *nekl-*
186 *3(sv3)*, or *mlt-4(sv9)* strong loss-of-function alleles, which typically arrest as partially constricted
187 L2/L3 larvae (Fig 1G). These results suggest that the mechanisms underlying the suppression of
188 molting defects by *adm-2* and CME-associated trafficking factors may be distinct.

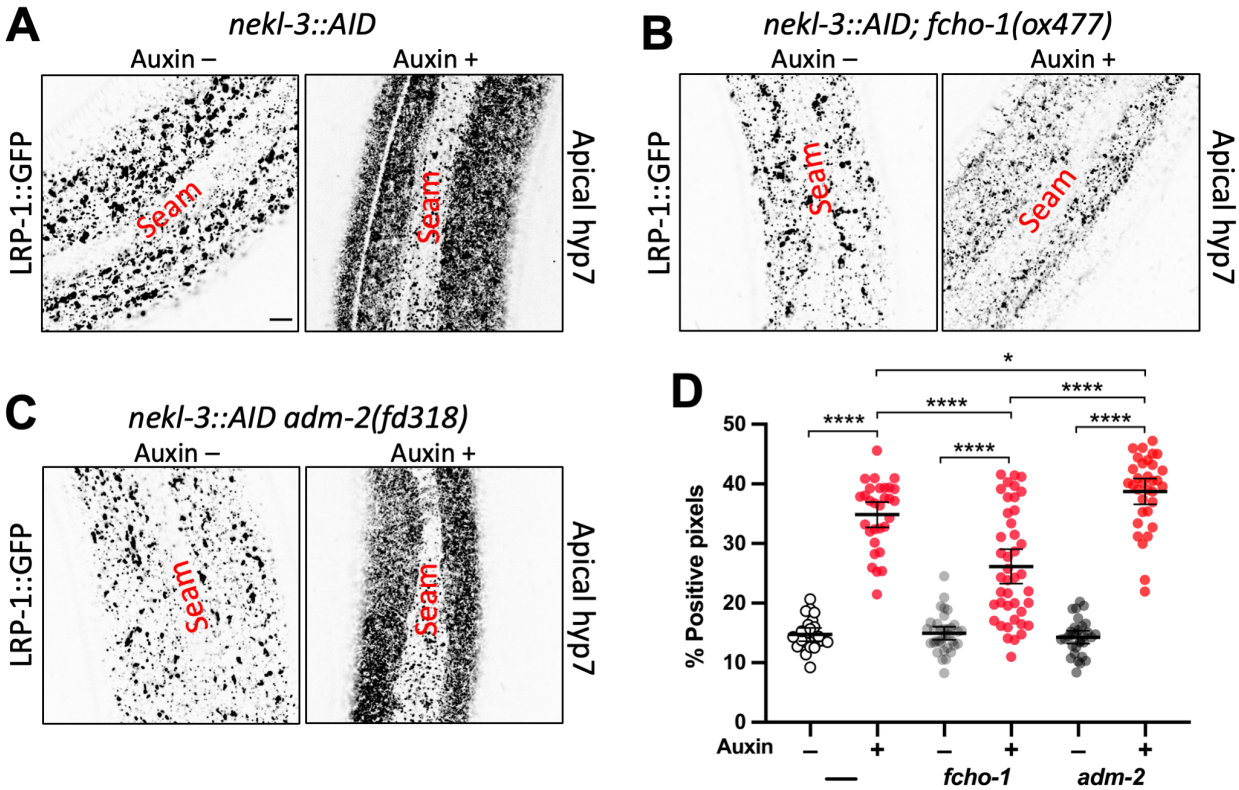

Fig 2. Loss of *adm-2* function does not correct the *nekl* trafficking defects
(A–C) Representative confocal images of 2-day-old adult worms expressing LRP-1::GFP in the apical hyp7 region of the epidermis. LRP-1 expression in the *nekl-3::AID* (A), *nekl-3::AID*; *fcho-1(ox477)* (B), and *nekl-3::AID; adm-2(fd318)* (C) mutant backgrounds in the absence (–) and presence (+) of auxin treatment. Bar in A = 5 μm (for A–C). (D) Dot plot showing the percentage of GFP-positive pixels within the apical plane of the worm epidermis for individuals of the specified genotypes and auxin treatment groups. Group means along with 95% confidence intervals (error bars) are indicated. p-Values were obtained by comparing means using an unpaired t-test: ****$p \leq 0.0001$, *$p \leq 0.05$.

189

190 To directly test if loss of ADM-2 can suppress CME defects in *nekls*, we examined the
191 localization of GFP-tagged LRP-1/megalin, an apical transmembrane cargo that is trafficked via
192 CME. Using the auxin-inducible degron (AID) system to remove NEKL-3 activity in 1-day-old
193 adult worms [11], we observed a dramatic accumulation of LRP-1::GFP at or near the apical
194 membrane (Fig 2A and 2D), consistent with our previous findings [11]. As anticipated, loss of

195 FCHO-1 partially corrected LRP-1::GFP mislocalization defects in NEKL-3::AID-depleted worms
196 (Fig 2B and 2D), consistent with the ability of *fcho-1* mutations to suppress *nekl*-associated
197 clathrin localization and mobility defects [11]. In contrast, complete loss of ADM-2 failed to
198 correct LRP-1::GFP defects in NEKL-3::AID-depleted adults and if anything showed slightly
199 enhanced apical LRP-1::GFP accumulation relative to the NEKL-3::AID-depleted worms (Fig 2C
200 and 2D; also see below). Collectively, these results indicate that ADM-2 does not suppress *nekl*
201 molting defects by correcting CME deficits and is therefore likely to act through a distinct
202 mechanism.
203
204 **ADM-2 is expressed in multiple tissues including the epidermis**
205 To gain insight into how ADM-2 may affect molting in *nekl* mutants, we examined endogenously
206 tagged *adm-2::mScarlet* and *adm-2::GFP* strains, in which the fluorescent marker was fused to
207 the C terminus of the ADM-2a cytoplasmic domain. Both CRISPR-tagged versions showed a
208 punctate pattern within hyp7, a large epidermal syncytium that encompasses most of the
209 central body region of the worm, including localization to small puncta near the apical
210 membrane (Fig 3A–E'). Notably, both NEKLs and MLTs are specifically expressed and required in
211 the hyp7 syncytium [8, 9]. We also detected some differences between the localization patterns
212 of ADM-2::mScarlet and ADM-2::GFP. In particular, ADM-2::mScarlet was observed in larger
213 vesicular and tubular-like structures throughout the epidermis, whereas these structures were
214 mostly absent in ADM-2::GFP worms (Fig 3A–D; also see below).
215
216 ADM-2 was also detectable in seam cells, a lateral epidermal syncytium that borders hyp7 along
217 the length of the animal (Fig 3E and 3E'); in the anterior epidermis (S3A and A'); and in a variety
218 of head, tail, and centrally located neurons (Fig 3E and 3E'; S3B–C and S3B'–C' Fig). In addition,
219 ADM-2 was observed in proximal oogenic cells of the hermaphrodite germline, with levels
220 increasing in maturing oocytes, where it was localized to the cytoplasm and plasma membrane
221 (Fig 3F and 3F'). Likewise, ADM-2 is expressed in fertilized oocytes (Fig 3F and 3F') and
222 throughout embryogenesis (S3D–F and S3D'–F' Fig). In contrast, ADM-2 was not detected in

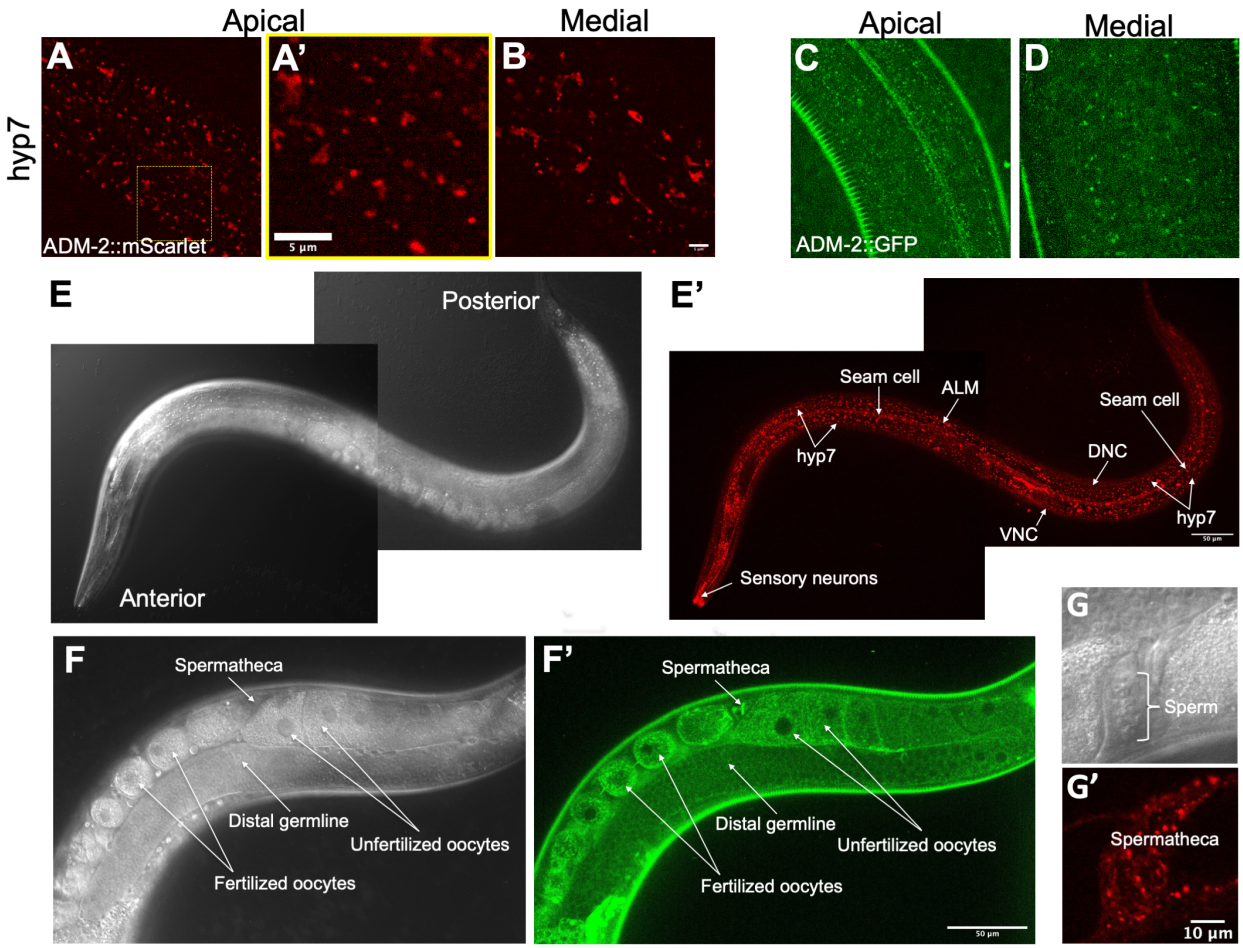

Fig 3. Expression of ADM-2 in the epidermis and other tissues
(A–D and A') Representative confocal images of ADM-2 expression in the *C. elegans* hyp7 region. ADM-2::mScarlet (A, B) and ADM-2::GFP (C, D) expression at apical (A, C) and medial (B, D) planes. A' is the inset from panel A. Bar in B = 5 µm (for A–D); in inset A' = 5 µm. (E–G and E'–G') Representative DIC (E–G) and confocal (E'–G') images of ADM-2 expression. ADM-2::mScarlet in the hyp7 hypodermis; seam cells; sensory neurons; and ALM, DNC, and VNC neurons (E, E') and in spermatheca (G, G'). ADM-2::GFP expression in the distal germline, oocytes, and spermatheca (F, F'). Bar in E' = 50 µm (for E, E'); in G' = 10 µm (for G, G'); in F' = 50 µm (for F, F').

mature sperm cells but was expressed in myoepithelial cells of the hermaphrodite spermatheca (Fig 3G and 3G'). We also note that ADM-2::GFP expression using a multicopy reporter under the control of the *adm-2* promoter region showed strongest expression in neurons where it accumulated at or near the plasma membrane (S3D Fig). These findings are consistent with ADM-2 acting in the epidermis to affect molting, but they also suggest that ADM-2 may have functions in other tissues.

ADM-2 is trafficked through endo-lysosomal compartments and is sensitive to NEKL activities

231 To determine the identity of ADM-2 puncta, vesicles, and tubular-like structures in the
232 epidermis, we performed colocalization experiments first using a CRISPR-tagged clathrin heavy
233 chain marker, GFP::CHC-1 [11]. Although statistically insignificant, rare colocalization between
234 ADM-2::mScarlet and apical clathrin was occasionally detected (Fig 4A–C', S4A Fig). We note
235 that endogenous plasma membrane–localized ADM-2::GFP and ADM-2::mScarlet both
236 presented with extremely faint signals within hyp7 (Fig 4A and 4C), making detection and
237 colocalization of this population difficult to assay; this suggests that ADM-2 may be rapidly
238 turned over at the plasma membrane, either by CME or through a CME-independent
239 mechanism. We note that mammalian ADAMs, including the meltrin family, are internalized via
240 CME [39-42]. In addition, we observed little or no colocalization between ADM-2::mScarlet and
241 medial GFP::CHC-1 clathrin-containing structures (S4C–E and S4C'–E' Fig), which may represent
242 clathrin-coated vesicles emanating from the trans Golgi or recycling endosomes.
243
244 In contrast, ADM-2::mScarlet exhibited partial colocalization with the endosomal marker
245 P_{hyp7}*::hgrs-1::GFP* in both the sub-apical and medial planes (Fig 4D–F', S4A–B, S4F–H and S4F'–
246 H' Fig). HGRS-1/HRS localizes to early endosomes and multivesicular bodies and is a component
247 of the ESCRT-0 complex, which, together with ESCRT-I–III, promotes cargo sorting and
248 lysosomal targeting [43-46]. Consistent with this, medial ADM-2::mScarlet showed strong co-
249 localization within the lysosomal marker LysoTracker Green during intermolts (Fig 4G–I), when
250 lysosomes appear roughly spherical, and during molting periods (Fig 4J–L), when lysosomes
251 acquire a tubular morphology [47]. Thus, following rapid uptake into endosomes, ADM-2 is
252 likely degraded by lysosomes, although some portion may be recycled back to the plasma
253 membrane. Degradation of ADM-2 by lysosomes is further supported by the relative absence of
254 medial ADM-2::GFP accumulation (Fig 3D), as GFP is acid sensitive and fluorescence is rapidly
255 quenched within maturing endosomes and lysosomes [47, 48].
256
257 Given our previous observations showing that NEKL–MLT proteins are required for normal
258 trafficking within hyp7 [8, 10, 11], we tested if depletion of NEKLs caused changes in the
259 abundance and subcellular localization of ADM-2. Notably, we observed total levels of ADM-

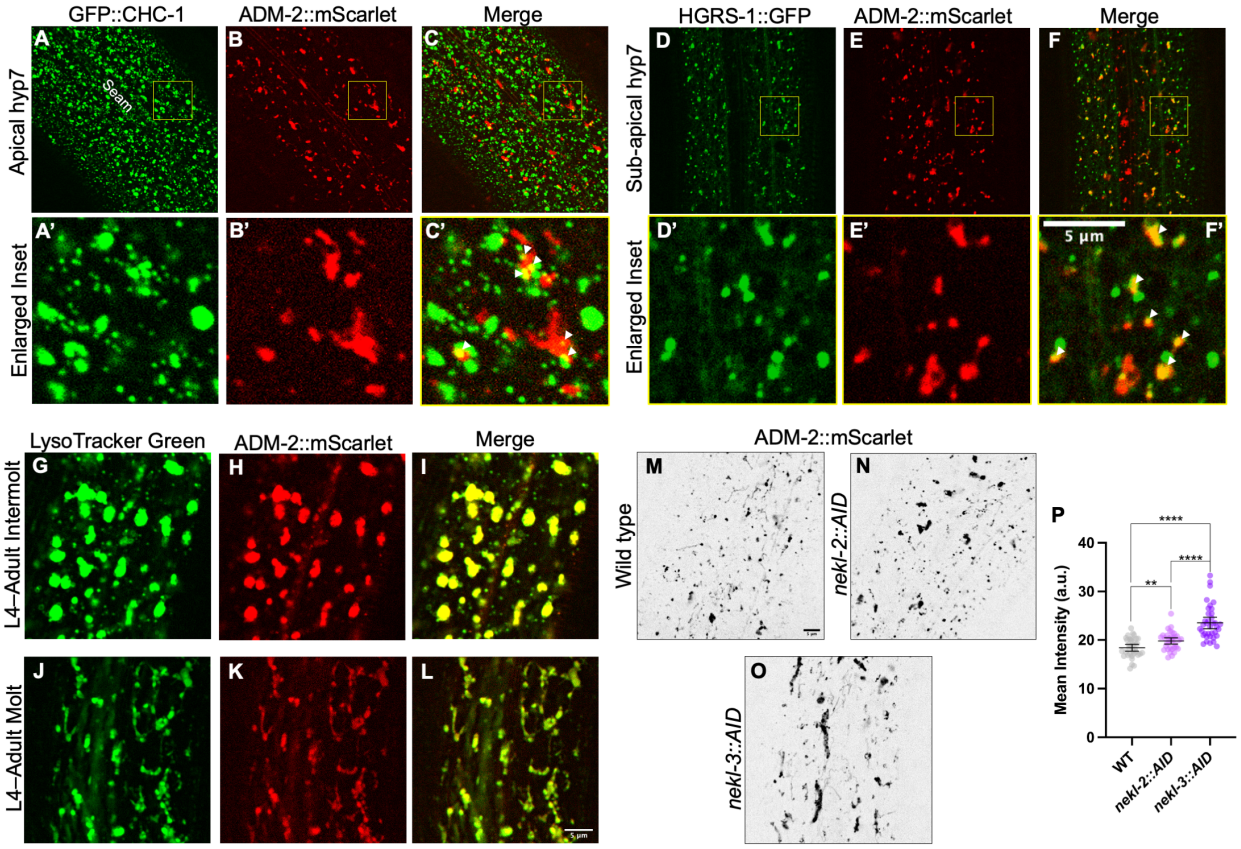

Fig 4. ADM-2 localization to endocytic compartments is affected by NEKL activity
(A–L) Co-localization analysis of ADM-2::mScarlet with GFP::CHC-1 (A–C), P_{hyp7}::HGRS-1::GFP (D–F), and LysoTracker Green (G–L) within apical (A–C) and sub-apical or medial (D–L) planes of hyp7. A'–F' are insets of A–F confocal images. White arrowheads in C' and F' indicate colocalized puncta. For LysoTracker studies (G–L), representative confocal images during intermolt (G–I) and molting (J–L) stages are shown. (M–P) Apical hyp7 ADM-2::mScarlet localization in auxin-treated wild-type (M), *nekl-2::AID* (N), and *nekl-3::AID* (O) 2-day-old adults with average mean intensity calculations (P). Group means along with 95% confidence intervals (error bars) are indicated. p-Values were obtained by comparing means using an unpaired t-test: ****p ≤ 0.0001, **p ≤ 0.01. Bar in M = 5 µm (for A–F and M–O); in F' = 5 µm (for insets A'–F'); in L = 5 µm (for G–L).

2::mScarlet to increase slightly in auxin-treated *nekl-2::AID* adults, with more robust changes occurring in auxin-treated *nekl-3::AID* animals (Fig 4M–P). Consistent with this, partial knockdown of MLT-3 in adults by RNAi led to modest increases in the levels of ADM-2::mScarlet and GFP::CHC-1 (S5A–B Fig). In worms that had undergone NEKL::AID depletion, ADM-2::mScarlet increased slightly in total levels and accumulated in large internal endocytic or lysosome-like structures (Fig 5M–P). Collectively, these findings indicate that NEKL activities impact ADM-2 trafficking within hyp7.

The protease domain of ADM-2 is critical for its function

269 Most ADAM family members, including the human meltrins, contain a catalytically active
270 metalloprotease domain that is distinguished by three conserved histidine residues
271 (HExxHxxGxxH) that coordinate the binding of zinc [49, 50]. To determine if the putative
272 metalloprotease activity of ADM-2 is critical for its influence on molting, we CRISPR-engineered
273 an ADM-2 variant in which the three conserved histidine residues within the predicted Zn-
274 binding domain were altered [Zn-MTP: H312–H322 (**HE**L**GH**TF**G**MD**H** > **DA**L**AY**TF**R**MD**Y**)] (Fig 5A
275 and 5B). Notably, this variant displayed robust suppression of *nekl-2; nekl-3* molting defects,
276 indicating that the protease function of ADM-2 is central to its function in molting and that its
277 loss is sufficient for *nekl* suppression (Fig 5C).
278
279 To further assess ADM-2 functional domains, we tested CRISPR variants designed to disrupt a
280 predicted N-terminal furin-cleavage site (NT-Furin: R149–R152 [**R**KK**R** > **V**KK**V**]) and a predicted
281 disintegrin motif (DM: E388–G396 (EPGE**ECDCG** > EPGE**VLADP**) (Fig 5A and 5B). Both variants
282 led to relatively weak suppression of *nekl-2; nekl-3*, suggesting that these domains are less
283 critical with respect to the molting-associated functions of ADM-2 (Fig 5C). Interestingly, a
284 variant that affects a predicted cysteine loop within the greater disintegrin domain (CysL: C438–
285 P459 [CRAAIGICDL**DEYCNG**ETNDCP > CRAAIGICDL**QQNGDH**ETNDCP]) strongly suppressed *nekl-*
286 *2; nekl-3* molting defects (Fig 5A–C). To better understand the basis for the observed
287 suppression patterns, we made use of the AlphaFold database [51, 52] to obtain the predicted
288 structure of ADM-2 and then performed homology modeling using the online Robetta protein
289 structure prediction service [53, 54] to model the effects of our mutations. Notably, whereas
290 the NT-furin and DM mutations were projected to have minimal impacts on the configuration
291 of histidine residues within the Zn-MTP domain (Fig 5D and 5E), the CysL variant was predicted
292 to substantially alter the position of His322, leading to an expected reduction in
293 metalloprotease activity (Fig 5F). Collectively, these data indicate that the protease domain of
294 ADM-2 is central to its impact on the molting process and that other N-terminal domains may
295 play more minor or indirect roles in this context.
296

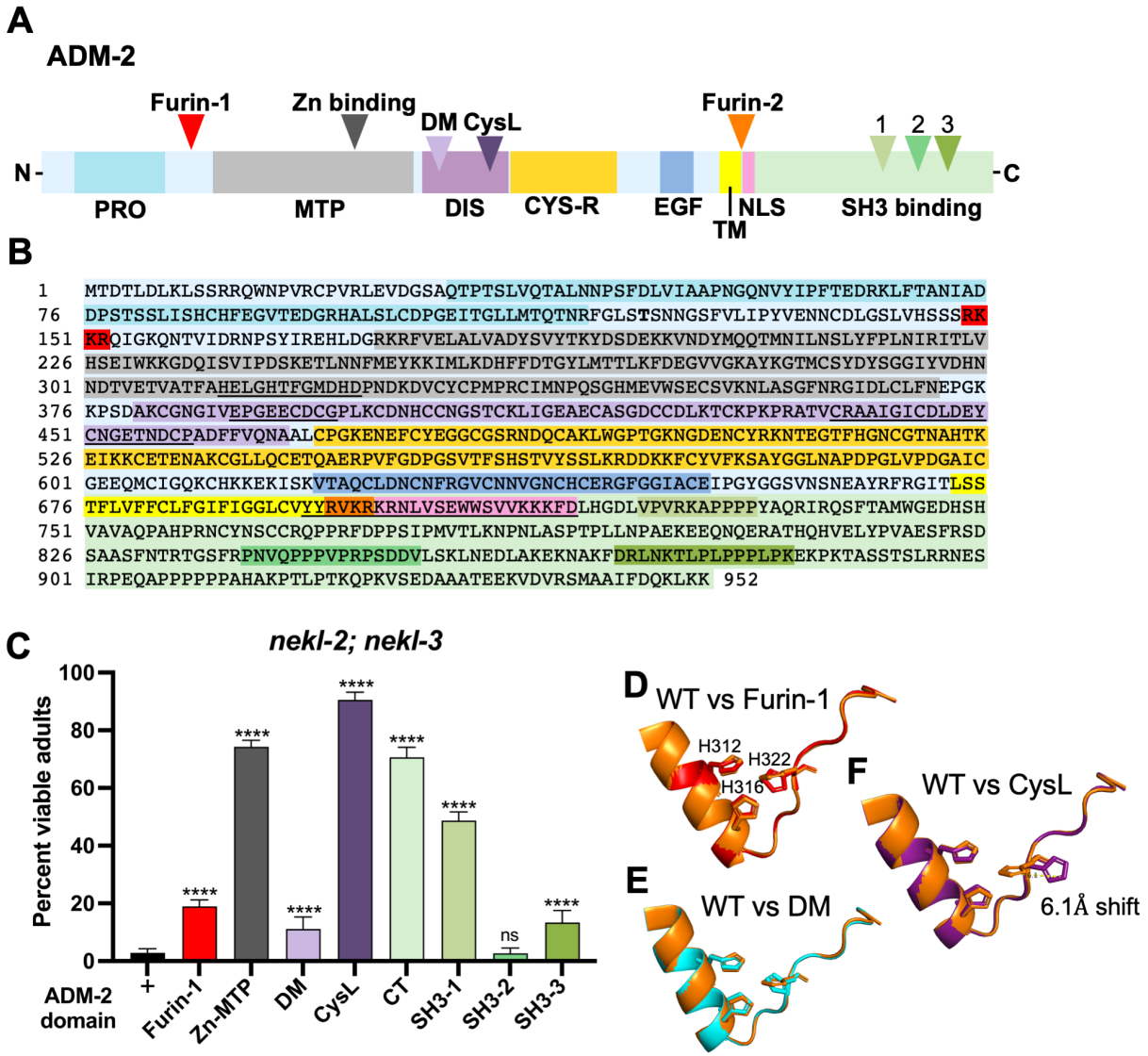

Fig 5. Functional analysis of ADM-2 domains
(A) Schematic representation of predicted protein domains within ADM-2. PRO, prodomain; MTP, metalloprotease domain; DIS, disintegrin domain; CYS-R, cysteine repeat region; TM, transmembrane domain; NLS, predicted nuclear localization signal; DM, disintegrin motif; CysL, cysteine loop; SH3 binding (1–3) Src homology 3 binding domains. (B) Color-coded peptide sequence of ADM-2 corresponding to panel A. For additional details see S2 Fig. (C) Percentage of viable (non-molting-defective) *nekl-2; nekl-3* adults in the indicated CRISPR-derived *adm-2* mutant backgrounds. Error bars represent 95% confidence intervals. p-Values were determined using Fisher's exact test: ****$p \leq 0.0001$; ns, not significant. (D–F) Predicted three-dimensional protein structures (for amino acid region 307–328) of wild-type ADM-2 (orange) superimposed on modeled structures for the Furin-1 (D; red), DM (E; cyan), and CysL (F; violet) mutant proteins. Three conserved histidine residues (His312, His316, His322) of the Zn-metalloprotease domain are represented as sticks. (F) A predicted 6.1-Å shift of the 'tele' nitrogen atom in the imidazole ring of His322 in the CysL mutant.

297 We also tested the importance of the ADM-2 C-terminal domain (R696–K952) using several
298 CRISPR-generated lines. Deletion of most of the C terminus (CT: ΔH718–M942) led to strong
299 suppression of *nekl-2; nekl-3* molting defects, whereas perturbation of individual SH3-binding
300 domains led to suppressive effects ranging from minimal (SH3-2: P839–V853

301 [**P**NVQ**PPP**V**PRP**S**DDV** > **G**NVQ**GAG**V**GAG**S**LLE**] and SH3-3: K874–K884 [**K**TL**P**L**PPP**L**PK** >
302 ITL**E**L**GAG**L**GL**]) to moderate (SH3-1: V722–P731 [**VP**V**RK**A**PPPP** > **EG**V**LA**A**GAVG**]) (Fig 5A–C). We
303 also note the presence of a potential fourth SH3-binding domain in the region of P907 (Fig 5b,
304 S2 Fig). As expected, none of the C-terminal mutations led to predicted changes in the
305 configuration of histidine residues in the Zn-binding domain (S6 Fig). A role for the C-terminus
306 in mediating ADAM function is not unexpected given that this domain is proposed to be
307 important for the regulation of cell signaling and subcellular localization and contains
308 specialized motifs that are thought to be involved in the 'inside-out' regulation of ADAM
309 metalloprotease activity [30, 31, 33, 55].
310
311 **Overexpression of ADM-2 causes molting defects**
312 Given that loss of ADM-2 did not lead to defects in molting but was capable of suppressing
313 molting defects in *nekl-2; nekl-3* mutants, we hypothesized that ADM-2 may normally exert an
314 inhibitory effect on the molting process. To test if ADM-2 is a negative regulator of molting, we
315 generated strains carrying the *adm-2* cDNA under the control of a heat shock–inducible
316 promoter ($P_{hsp\text{-}16}$*::adm*-2 and $P_{hsp\text{-}16}$*::adm-2::GFP*. Strikingly, when subjected to heat shock
317 during larval development (i.e., overexpression of *adm-2*), we observed molting defects in
318 ~50% of larvae carrying these heat-shock–ADM-2 transgenes (Fig 6A and 6D). In contrast,
319 molting defects were not observed in heat-shocked controls or in non-heat-shocked worms (Fig
320 6A); ADM-2::GFP expression was specifically detected in heat-shocked worms only (Fig 6B and
321 6C). In addition, we observed a low frequency of blister phenotypes in animals that
322 overexpressed ADM-2::GFP, a defect associated with detachment of the cuticle from the
323 epidermis (Fig 6E). These findings are consistent with ADM-2 playing an inhibitory role in
324 molting and suggest that ADM-2 may also influence attachment of the epidermis to the cuticle.
325
326 **ADM-2 is a negative regulator of LRP-1/megalin**
327 ADAM/meltrin family proteins function as "sheddases", cleaving target peptides that are
328 positioned at or near the outer leaflet of the plasma membrane [30, 31, 56-70]. Given our
329 above findings, we hypothesized that ADM-2 may function as a sheddase for one or more apical

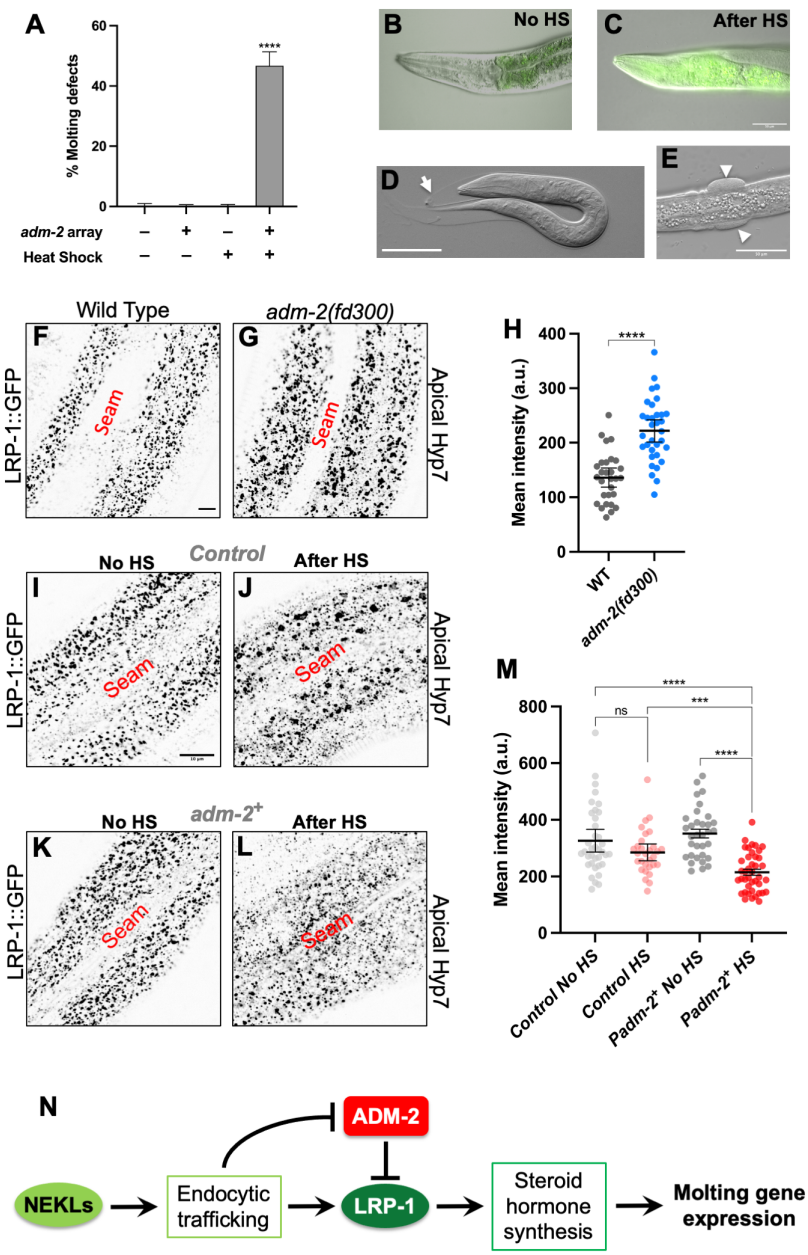

Fig 6. ADM-2 is a negative regulator of molting and LRP-1
(A) Bar plot showing the percentage of molting defects in the specified strains in the presence and absence of the $P_{hsp\text{-}16}$*::adm-2::GFP* transgene in the wild-type background and in the presence and absence of heat shock. Error bars represent 95% confidence intervals. p-Values were determined using Fisher's exact test: ****p ≤ 0.0001. (B,C) Merged DIC and fluorescence images of an adult worm carrying the $P_{hsp\text{-}16}$*::adm-2::GFP* transgene in the absence of heat shock (B) and after heat shock (C). (D) Molting-defective larva after heat shock. White arrow in D indicates unshed old cuticle. (E) Rare blister phenotype in a worm after ADM-2::GFP induction. White arrowheads in E indicate blisters. Bar in C = 50 μm (for B and C); in D = 50 μm; in E = 50 μm. (F,G) Representative confocal images of 1-day-old adult wild-type (F) and *adm-2(fd300)* (G) worms expressing LRP-1::GFP in the hyp7 region of the hypodermis. Bar in F = 5 μm (for F,G). (H) Dot plot showing LRP-1::GFP mean intensity (a.u.) within the apical plane of the worm hypodermis for each individual worm of the specified genotype. (I–L) Representative confocal images of 1-day-old adult worms expressing LRP-1::GFP in the hyp7 region of the hypodermis. (I,J) LRP-1 expression in wild-type control worms. (K,L) LRP-1 expression in worms containing the $P_{hsp\text{-}16}$*::adm-2* transgene. Worms are shown in the absence of heat shock (I,K) and after heat shock (J,L). Bar in I = 10 μm (for I–L). (M) Dot plot showing LRP-1::GFP mean intensity (a.u.) within the apical plane of the worm hypodermis for each individual worm of the specified genotype and heat shock conditions. In H and M, group means along with 95% confidence intervals (error bars) are indicated. p-Values were obtained by comparing means using an unpaired t-test: ****p ≤ 0.0001; ***p ≤ 0.001; ns, p ≥ 0.05. (N) Genetic model of ADM-2 function in *C. elegans* molting.

membrane proteins that positively regulate the molting process. As such, loss of ADM-2 may lead to the upregulation or de-repression of these proteins, thereby alleviating molting defects in weak *nekl* loss-of-function mutants. One candidate protein for regulation by ADM-2 is LRP-1, a positive regulator of molting and a known target of NEKL trafficking (also see above) [71-79]. Notably, two mammalian homologs of LRP-1 (LRP1/LRP2) are negatively regulated by matrix metalloproteinases and ADAM family members, including the meltrin ADAM12 [71-81]. To test this possibility, we examined levels of LRP-1::GFP in *adm-2* null mutants and observed apical

337 levels of LRP-1::GFP to be ~1.6-fold higher in *adm-2* mutants relative to wild type (Fig 6F–H). In
338 contrast, loss of *adm-2* did not alter the levels of a clathrin heavy chain reporter at the apical
339 membrane (S7A–D Fig), indicating that ADM-2 does not generally affect CME.
340
341 To further examine the relationship between ADM-2 and LRP-1 we tested the effects of ADM-2
342 overexpression on LRP-1::GFP levels. One-day-old adult worms carrying the $P_{hsp\text{-}16}$*::adm-2*
343 transgene and LRP-1::GFP were heat shocked, and LRP-1::GFP levels were assayed ~2–3 hours
344 later. Whereas heat shock alone did not significantly alter LRP-1::GFP levels in the absence of
345 the P_{HS}*::adm-2* transgene, levels of LRP-1::GFP were ~1.6-fold lower when worms containing
346 the P_{HS}*::adm-2* transgene were heat shocked relative to non-heat-shocked controls (Fig 6I–M).
347 These striking reciprocal findings are consistent with ADM-2 functioning as a negative regulator
348 of LRP-1 and suggest that suppression by loss of functional ADM-2 may occur in part through
349 the upregulation or de-repression of cargo including LRP-1.
350
351 **Discussion**
352 In this study we demonstrated a unique role for the sole *C. elegans* meltrin family member,
353 ADM-2, as a negative regulator of the molting process. Whereas loss of ADM-2 did not overtly
354 impact the molting cycle, overexpression of ADM-2 during larval development did lead to
355 molting defects and larval arrest. Moreover, our previously described non-biased forward
356 genetic screen identified two independent loss-of-function alleles of *adm-2* as suppressors of
357 larval arrest and molting defects in *nekl-2; nekl-3* mutants [29]. Previous studies have
358 implicated proteases as positive regulators of molting including NAS-36, NAS-37, CPZ-1, and
359 SURO-1 [82-87]. Extracellular proteases have been suggested to be important for the
360 detachment and degradation of the old cuticle and may also play a dynamic role in ECM
361 remodeling during new cuticle synthesis [2]. Interestingly, roles for protease inhibitors in
362 molting have also been reported, as loss of the Kunitz domain–containing protease inhibitors
363 MLT-11 and BLI-5 lead to molting defects [83, 88, 89]. Protease inhibitors have been suggested
364 to be important for temporally or spatially restricting the activity of extracellular proteases
365 during the molting cycle. Consistent with this, epidermally expressed proteases and protease

366 inhibitors are highly enriched among genes that are transcriptionally regulated with the molting
367 cycle, indicating tight control of their proteolytic activity [90, 91].
368
369 Although we previously reported the suppression of *nekl* molting defects by mutations affecting
370 genes closely connected to CME, our data do not support a role for ADM-2 in the regulation of
371 intracellular trafficking per se. Rather, our findings are consistent with ADM-2 being a cargo of
372 CME, including during its passage through endosomes and its turnover in lysosomes. Moreover,
373 we observed increased levels of ADM-2 after NEKL knockdown along with the retention of
374 ADM-2 in intracellular compartments of the epidermis. Collectively these findings suggest that
375 loss of NEKL functions may lead to increased or aberrant ADM-2 activity, which may contribute
376 to molting defects in these mutants.
377
378 Notably, we identified LRP-1 as a candidate target of ADM-2 sheddase activity. Epidermal LRP-1
379 levels were increased in *adm-2* null mutants and were reduced when ADM-2 was
380 overexpressed. Moreover, alteration of the ADM-2 metalloprotease domain was sufficient to
381 mediate strong suppression of *nekl* molting defects, indicating that proteolytic/sheddase
382 activity is central to the effects of ADM-2 on molting. Notably, human LRP1 is a known target
383 for cleavage by ADAM10, ADAM12, and ADAM17 [71-79]. Moreover, after cleavage by ADAMs,
384 the solubilized extracellular domain of LRP1 retains its ability to bind apolipoproteins with high
385 affinity. This was proposed to decrease the effective concentration of ligand available for
386 internalization by membrane-bound LRP1, leading to a reduction in cholesterol internalization
387 [80]. In addition, matrix metalloproteases have been proposed to mediate the cleavage and
388 proteolysis of mammalian LRP2/megalin, although the identity of the protease(s) was not
389 determined [77-81]. Given that *C. elegans* LRP-1 is most similar to mammalian LRP2, our study
390 suggests that LRP2 may be regulated by meltrin family members. Together, our data are
391 consistent with ADM-2 playing a conserved role in the repression of LRP family members.
392
393 Our findings, together with published data from our lab and other research groups, point to a
394 working model in which epidermal intracellular trafficking may play two roles in the molting

395 process (Fig 6N). Based on previous studies, endocytosis is required for the internalization of
396 factors required for molting, such as steroid hormone precursors [5, 6], and may also be
397 important for recycling old cuticle components, such as collagens [47, 92]. This function is
398 consistent with our recent observation that loss of *nekls* leads to defects in the transcriptional
399 upregulation of those molting genes for which their expression depends on the activation of
400 nuclear hormone receptors [12]. In addition, endocytosis may also be required for the uptake
401 and degradation of cargo that would otherwise exert an inhibitory effect on molting. Impaired
402 endocytic trafficking in *nekl* mutants may simultaneously lead to a reduction in cholesterol
403 uptake via LRP-1 and an increase in the levels of a negative regulator of LRP-1, ADM-2 (Fig 6N).
404 In this model, loss of *adm-2* would lead to de-repression of LRP-1, and possibly other positive
405 effectors of molting, thereby compensating for a partial loss of NEKL trafficking functions. In
406 contrast, when NEKL functions are severely reduced, loss of ADM-2 would not be expected to
407 offset a more severe deficiency in the uptake of steroid precursors, consistent with our
408 observation that *adm-2* mutations do not suppress strong loss-of-function alleles in *nekls*. In
409 summary, our findings expand the roles for NEKLs and intracellular trafficking in the molting
410 process and implicate ADM-2 as a negative regulator of the molting process.
411
412
413 **Materials and Methods**
414 **Strains.** *C. elegans* strains were maintained according to standard protocols [93] and were
415 propagated at 22°C, unless stated otherwise. Strains used in this study are listed in S1 Table.
416
417 **Transgenic Rescue.** Fosmids containing rescuing sequences for *adm-2*/C04A11.4
418 (WRM0620dD12, WRM0632aG02, and WRM0610cA04, 2–6 ng/µl each + *sur-5::RFP* [pTG96],
419 50–100 ng/µl) were injected into strain WY1342. Stable strains (WY1386 and WY1388)
420 containing rescuing arrays for both *nekl-3* (*fdEx286*; GFP^+) and *adm-2* (*fdEx315* or *fdEx356*;
421 RFP^+) were scored to determine the percentage of viable RFP^+ progeny.
422

423 **Determination of dominant versus recessive alleles.** To distinguish between dominant and
424 recessive alleles, we first crossed suppressed *nekl-2*(*fd81*); *nekl-3*(*gk894345) fd130*
425 hermaphrodites to WY1145 [*nekl-2*(*fd81*); *nekl-3*(*gk894345); fdEx286 (nekl-3*$^{+}$ *+ sur-5::GFP)*]
426 males and scored for suppression of GFP^{-} cross-progeny males. For *fd130* and *fd162*, 50/96 and
427 30/52 viable cross-progeny adult males were GFP^{-}, respectively, indicating that these mutations
428 are either dominant or on LGX. We next crossed *nekl-2*(*fd81*); *nekl-3*(*gk894345) fd130*
429 hermaphrodites to WY1232 [*nekl-2*(*fd81*); *nekl-3*(*gk894345*); *fdEx186* (*nekl-3*$^{+}$ + *sur-5::GFP*);
430 *fdEx197 (sur-5::RFP)*] males and scored for suppression of GFP^{-} RFP^{+} cross-progeny
431 hermaphrodites. In the case of cross-progeny *fd130/+* adult hermaphrodites, 62/62 were either
432 GFP^{+} RFP^{-} or GFP^{+} RFP^{+}; no GFP^{-} RFP^{+} adults were observed. Similarly, 182/185 *fd162/+* adult
433 hermaphrodites were either GFP^{+} RFP^{-} or GFP^{+} RFP^{+}, and only 3/185 were GFP^{-} RFP^{+}. Given the
434 ~98.5% penetrance of *nekl-2*(*fd81*); *nekl-3*(*gk894345)* larval lethality [29], our results indicate
435 that *fd130* and fd162 are fully recessive but are on LGX.
436
437 **RNAi.** Primers containing the binding motif for T7 RNA polymerase (5'-
438 TAATACGACTCACTATAGGGAGA-3') and corresponding to *adm-2* (5'-
439 GACCACAACAATGATACGGTCGAA-3'; 5'-CCTGGACACAATGCAGCATTTTGA-3'), *unc-71* (5'-
440 TGTCGTCGACGGTTCCGAAGA-3'; 5'-GCATCAGACAGACCAGGCATAG-3'), *adm-4* (5'-
441 ATGCATTCAATACACGTGTGA-3'; 5'-CTTCCTCTCCCAGATATATCGT-3'), *sup-17* (5'-
442 AGTGTCAACCTGGTCTTCCTG-3'; 5'-CTGTGCCCATTGTGTTAGAGTTTC-3'), *mig-17* (5'-
443 CTCAGCTACACAAGGAATGGC-3'; 5'-TTCGCACACGTTCTACAACA-3'), *tag-275* (5'-
444 TGTTCTCGCGTCATTCGTTGC-3'; 5'-ACTCGGTTTATTGGAACATTTGGC-3'), *F27D9.7 (*5'-
445 CAACATTCTGTGCGATGCGGT-3'; 5'-TTAAATGGGCGCGACAGATCC-3'), *adt-1* (5'-
446 GTCAGTGCACTCACTGGACAT-3'; 5'-GGTTAGGCATGGCCTGAATCT-3'), *adt-2* (5'-
447 GAAGACGAAACCGAAGTCTGC-3'; 5'-TTACCTCCCCATGCAGCATTT-3'), *adt-3* (5'-
448 CAGGTATGTAACGGTGACTCCA-3'; 5'-CATTACACATGGTCCGGTTTC-3'), and *gon-1* (5'-
449 TGGATCACTGAAGATGTGTCT-3'; 5'- GCACTCCAATCAGTATTTCTC-3') were used to generate
450 dsRNA using standard methods [94]. After injection at 0.8–1.0 µg/µl into WY1145
451 hermaphrodites, F1 progeny were scored for adult viability. For RNAi feeding experiments, the

452 relevant bacterial strains were obtained from Geneservice and IPTG (8 mM) was added to
453 growth plates [95]. Worm strains were grown on *lin-35(RNAi)* plates for two generations to
454 increase RNAi susceptibility [96]. Second-generation fourth larval stage (L4) worms growing on
455 *lin-35(RNAi)* plates were transferred to experimental plates and were imaged after 48 hours.
456 RNAi feeding experiments were performed at 20°C.
457
458 **ADM-2 CRISPR mutant alleles.** Design of repair sequences containing introduced restriction
459 sites was facilitated using CRISPRcruncher [97]. For details on primers sequences see S2 File.
460 Strong loss-of-function alleles. Alleles *fd228–fd230* and *fd235–fd237* were generated using
461 guide dual sequences SB1 and SB2, PCR amplification primers SB3 and SB4, and the sequencing
462 primer SB6. In *fd228–fd230* and *fd235–fd237*, an ~3.2-kb region spanning *adm-2a* exons 3–9 is
463 deleted. *fd228* is an indel predicted to encode sequences through T122 of ADM-2a, followed by
464 eight divergent amino acids and a stop codon. *fd229* is an indel predicted to encode sequences
465 through S123 of ADM-2a, followed by a stop codon. *fd230* is an indel predicted to encode
466 sequences through T122 of ADM-2a, followed by a stop codon. *fd235* is an indel predicted to
467 encode sequences through T122 of ADM-2a, followed by 23 new amino acids and a stop codon.
468 *fd236* is an indel predicted to encode sequences through F118 of ADM-2a, followed by six new
469 amino acids and a stop codon. *fd237* is an indel predicted to encode sequences through T122 of
470 ADM-2a, followed by a single new amino acid and a stop codon. Alleles *fd298–302* were
471 generated using guide sequences SB46 and SB47, PCR amplification primers SB48–SB51, and
472 the sequencing primer SB52. In *fd298–fd302*, *fd313*, *fd316*, and *fd317* an ~7.4-kb region
473 spanning *adm-2a* exons 1–19 is deleted. *fd298* is an indel that encodes sequences through T2 of
474 ADM-2a followed by four new amino acids and a stop codon. *fd299* is a deletion that encodes
475 sequences through M1 of ADM-2A, followed by three new amino acids and a stop codon. *fd300*
476 is an indel that encodes sequences through D3 of ADM-2a, followed by 14 new amino acids and
477 a stop codon. *fd301* and *fd302* are identical indels that encode sequences through D3 of ADM-
478 2a, followed by 12 new amino acids and a stop codon. *fd313* encodes sequences through T2 of
479 ADM-2a, followed by 40 new amino acids and a stop codon. *fd316* deletes the normal start
480 codon; an alternative ATG is predicted to encode 24 new amino acids followed by a stop codon.

481 *fd317* encodes sequences through D3 of ADM-2a, followed by 16 new amino acids and a stop
482 codon. *fd318* encodes sequences through D3 of ADM-2a, followed by 8 new amino acids and a
483 stop codon.
484 *adm-2* metalloprotease mutation (Zn-binding domain). Alleles *fd243–fd247* were generated
485 using the guide sequence SB27, the repair template Rep2, PCR amplification primers SB28 and
486 SB29, and sequencing primers SB31 and SB32. *fd243–fd247* change the predicted ADM-2a Zn-
487 metalloprotease active site spanning H312–H322 (**HE**L**GH**TF**G**MD**H**) to **DA**L**AY**TF**R**MD**Y** (altered
488 aa are in bold). The Zn-metalloprotease consensus motif is HEXXHXUGUXH, where U is an
489 amino acid containing a bulky hydrophobic residue. The edited locus contains an introduced
490 BstBI site.
491 *adm-2* disintegrin motif mutation. Allele *fd322* was generated using guide sequence DF1, the
492 repair template Rep9, PCR amplification primers DF2 and DF3, and sequencing primers DF4 and
493 DF5. *fd322* changes the predicted ADM-2a disintegrin motif (DM) spanning E388–G396
494 (EPGE**ECDCG**) to EPGE**VLADP**. The edited locus contains introduced NheI and BamHI sites.
495 *adm-2* cysteine loop mutation. Alleles *fd324–fd325* were generated using guide sequence DF6,
496 the repair template Rep10, PCR amplification primers DF2 and DF3, and sequencing primers
497 DF4 and DF5. *fd324–fd325* change the predicted ADM-2a cysteine loop (CysL) spanning C438–
498 P459 (CRAAIGICDL**DEYCNG**ETNDCP) to CRAAIGICDL**QQNGDH**ETNDCP. The edited locus contains
499 an introduced PstI site.
500 *adm-2* furin 1 mutation. Alleles *fd288-fd290* were generated using guide sequence SB17, the
501 repair template Rep6, PCR amplification primers SB18 and SB19, and sequencing primers SB20
502 and SB21. *fd288-fd290* change the predicted ADM-2a furin-1 cleavage site spanning R149–R152
503 (**R**KK**R**) to **V**KK**V**. The edited locus contains an introduced BamHI site.
504 *adm-2* SH3-binding domain 1 mutation. Alleles *fd248–fd251* were generated using the guide
505 sequence SB32, the repair template Rep3, PCR amplification primers SB16 and SB34, and
506 sequencing primer SB35. *fd248–fd251* alter the predicted ADM-2a SH3-1 domain spanning
507 V722–P731 (**VP**V**RK**A**PPPP)** to **EG**V**LA**A**GAVG**. The edited locus contains an introduced XhoI site.
508 *adm-2* SH3-binding domain 2 mutation. Alleles *fd252–fd256* were generated using the guide
509 SB36, the repair template Rep4, PCR amplification primers SB37 and SB38, and sequencing

510 primers SB39 and SB40. *fd252–fd256* alter the predicted ADM-2a SH3-binding domain 2 domain
511 spanning P839–V853 (**P**NVQ**PPP**V**PRP**S**DDV**) to **G**NVQ**GAG**V**GAG**S**LLE**. The edited locus contains
512 an introduced XhoI site.
513 <u>*adm-2* SH3-binding domain 3 mutation.</u> Alleles *fd257–fd259* were generated using the guide
514 sequence SB41, the repair template Rep5, PCR amplification primers SB37 and SB38, and
515 sequencing primers SB39 and SB40. *fd257–fd259* alter the predicted ADM-2a SH3-binding
516 domain 3 spanning K874–K884 (**K**TL**P**L**PPP**L**PK**) to **I**TL**E**L**GAG**L**GL**. The edited locus contains an
517 introduced XhoI site.
518 <u>*adm-2* C-terminal (cytoplasmic domain) deletion.</u> Alleles *fd231–fd234* were generated using the
519 guide sequences SB12 and SB13, the repair template Rep1, PCR amplification primers SB14 and
520 SB15, and sequencing primer SB16. *fd231–fd234* remove sequences from H718 to M942 of
521 ADM-2a and introduce a XhoI site.
522
523 **ADM-2 expression plasmids and strains.** *adm-2::GFP* and *adm-2::mScarlet* endogenously
524 tagged strains were made using CRISPR/Cas9 technology in collaboration with SunyBiotech
525 Corporation (China). Expression vectors were generated by amplifying the *adm-2* promoter
526 region from fosmid WRM0620dD12 using primers SB57 and SB58. After digestion with SphI and
527 SalI, the ~2.1-kb PCR product was inserted into pPD95.75 to create pDF403–pDF405. *adm-2*
528 cDNA was amplified from plasmid pDONR201 (Horizon Inc.) using primers SB59 and SB60.
529 Digestion and ligation of the ~2.8-kb PCR product and pDF403 with XmaI and KpnI generated
530 pDF417–pDF420, which were confirmed by sequencing. pDF417 (~100 ng/µl) was injected into
531 N2 worms with *sur-5::RFP* (~50 ng/µl) to obtain lines carrying extrachromosomal arrays
532 (*fdEx353*, *fdEx354*). CRISPR-tagged *adm-2::mScarlet* and *adm-2::GFP* strains contain codon
533 optimized fluorescent-reporter insertions just preceding the *adm-2a* stop codon (SUNY
534 biotech). In addition, sequences upstream of the stop codon contain the indicated (bold) silent
535 mutations (LGX 13695343–13695387).
536 TC**T**GAAGATGCAGCTGCAACCGAAGAAAAAGTAGATGTTCGCTC**C** (wild type)
537 TC**A**GAAGATGCAGCTGCAACCGAAGAAAAAGTAGATGTTCGCTC**G** (CRISPR tagged)
538

539 ***adm-2* and *adm-2::GFP* heat shock strains.** An ~4.6-kb *adm-2::GFP::unc-54* 3'UTR cDNA
540 product was obtained by digesting pDF420 with XbaI and ApaI enzymes. Digestion of heat shock
541 vectors pPD49.78 and pPD49.83 was performed using NheI and ApaI to obtain an ~3-kb vector
542 backbone. Ligation of the *adm-2* cDNA with vector backbones pPD49.83 and pPD49.78
543 generated pDF429–pDF431 and pDF432–pDF434, respectively. Likewise, an ~2.8-kb *adm-2::GFP*
544 product was obtained by digesting pDF420 with XbaI and KpnI enzymes. Digestion of heat shock
545 vectors pPD49.78 and pPD49.83 was performed using NheI and KpnI to obtain an ~3-kb vector
546 backbone. Ligation of *adm-2::GFP* with vector backbones pPD49.83 and pPD49.78 generated
547 pDF423–pDF425 and pDF426–pDF428, respectively. pDF430 and pDF433 (50 ng/µl each) were
548 injected into N2 with pRF4 [*rol-6(gf)*] (~50 ng/µl) to obtain lines carrying extrachromosomal
549 arrays (N2: *fdEx373–375*). Likewise, pDF424 and pDF425 (50 ng/µl each) were injected into N2
550 with pRF4 [*rol-6(gf)*] (~50 ng/µl) to obtain lines carrying extrachromosomal arrays (*fdEx381,*
551 *fdEx382*).
552
553 **Heat shock methods.** For Fig 6A, all worm strains were synchronized using bleach.
554 Synchronized L1 worms were plated on NGM plates and grown at 20°C for 2 hours. The plates
555 were then incubated at 34°C for 4 hours, after which they were shifted back to 20°C for 20
556 hours. The plates were shifted again to 34°C for 4 hours and were subsequently grown at 20°C
557 for 20–24 hours before the percentage of molting-defective worms was determined. For Fig 6I–
558 L, 1-day-old adult worms grown at 20°C were heat shocked at 34°C for 4 hours and were shifted
559 to 20°C for 2–3 hours before imaging.
560
561 **Protein domain identification and alignment tools.** The following sites were used to identify
562 domains within ADM-2 and human ADAM homologs:
563 http://nls-mapper.iab.keio.ac.jp/cgi-bin/NLS_Mapper_form.cgi
564 https://www.ncbi.nlm.nih.gov/Structure/cdd/wrpsb.cgi
565 https://www.ebi.ac.uk/interpro/
566 https://prosite.expasy.org/
567 https://psort.hgc.jp/form2.html

568 http://www.cbs.dtu.dk/services/TMHMM/
569 http://www.cbs.dtu.dk/services/SignalP/
570 http://phobius.sbc.su.se/
571 http://tcoffee.crg.cat/apps/tcoffee/do:regular
572 https://embnet.vital-it.ch/software/BOX_form.html
573
574 **Image acquisition.** Fluorescence images in the following figure panels—Fig 2A–C; Fig 6F–G; S3G
575 Fig; and S7 Fig—were acquired using an Olympus IX81 inverted microscope with a Yokogawa
576 spinning-disc confocal head (CSU-X1). Excitation wavelengths were controlled using an acousto-
577 optical tunable filter (ILE4; Spectral Applied Research). MetaMorph 7.7 software (MetaMorph
578 Inc.) was used for image acquisition. z-Stack images were acquired using a 100×, 1.40 N.A. oil
579 objective. Fig 3A–G; Fig 3A'–G'; Fig 4A–L; Fig 6I–L; S3A–F Fig; S3A'–F' Fig; and S4C–H Fig were
580 acquired using an Olympus IX83 inverted microscope with a Yokogawa spinning-disc confocal
581 head (CSU-W1). z-Stack images were acquired using a 100×, 1.40 N.A. silicone oil objective.
582 cellSense3.1 software (Olympus corporation) was used for image acquisition. DIC images in the
583 panels Fig 1A–C and Fig 7B–E were acquired using a Nikon Eclipse epiflourescence microscope
584 and the cellSense3.1 software (Olympus corporation).
585
586 **Image analysis.** Mean intensity (measured in arbitary units, a.u.), percent of fluorescence-
587 positive pixels above threshold, and the colocalization analysis were performed using Fiji
588 software (NIH; available at https://imagej.net/Fiji/Downloads). For a given z-plane of interest,
589 rolling ball background subtraction was performed (radius = 50 pixels), and the polygon
590 selection tool was used to choose the region of hyp7 in which the mean intensity was
591 quantified (Fig 4, Fig 6, S5 Fig, and S7 Fig). The percentage of fluorescence-positive pixels for the
592 region of interest (Fig 2) was determined after thresholding, and the "Huang" thresholding
593 algorithm was used for strain comparisons. For colocalization, rolling ball background
594 subtraction was performed (radius = 25 pixels), followed by use of the mean filter (radius = 2
595 pixels) to minimize noise. Finally, the same thresholding algorithm was used for one particular
596 channel to obtain binary images to be used as masks (GFP::CHC-1 and HGRS-1::GFP—"Otsu";

597 ADM-2:mScarlet—"Isodata"). This binary mask was combined using the "AND" boolean
598 operation to the original image and the combined image was used for the colocalization
599 analysis. Data from Fig 6F and 6G (Olympus IX81) and Fig 6I–L (Olympus IX83) were obtained on
600 different confocal microscopes and thus differ in their mean intensity values.
601
602 **Auxin treatment.** Auxin (indole-3-acetic acid) was purchased from Alfa Aesar. A 100× stock
603 auxin solution (0.4 M) was made by dissolving 0.7 g of auxin in 10 ml of 100% ethanol. A
604 mixture of 25 µl of stock auxin solution and 225 µl of distilled water was added to plates
605 containing 1-day-old adult worms.
606
607 **Protein 3D structure analysis.** PDB file (Identifier : AF-G5EDW5-F) containing the three-
608 dimensional structure details of *C. elegans* ADM-2 was obtained from the AlphaFold database (
609 https://alphafold.ebi.ac.uk/) [51, 52]. Using the AlphaFold structure as template, homology
610 modeling was performed by the online Robetta structure prediction server
611 (https://robetta.bakerlab.org/) to obtain the predicted the three-dimensional structures of the
612 respective ADM-2 mutants [53, 54]. For modeling CM (Comparative modeling) option was used
613 and the number of models to sample was selected as 1. Other options remained unchanged.
614 The homology modeled three-dimensional structures were rendered, and was superimposed
615 onto the AlphaFold structure of ADM-2 using the PyMOL 2 software (The PyMOL Molecular
616 Graphics System, Version 2.0 Schrödinger, LLC.).
617
618 **Statistical analyses.** Statistical analyses were carried out using Prism software (GraphPad)
619 following established standards [98].
620
621 **Acknowledgements**
622 We thank Amy Fluet for editing this manuscript and Barth D. Grant for the HGRS-1 marker
623 strain. This project was supported by R35 GM136236 to DSF and by an Institutional
624 Development Award (IDeA) from the National Institute of General Medical Sciences of the
625 National Institutes of Health (P20GM103432).

626 ## Figure Legends

627 **Fig 1. Loss of ADM-2 function suppresses *nekl* molting defects**

628 (A) DIC image of *nekl-2; nekl-3* double-mutant worms. The adult worm contains a rescuing
629 extrachromosomal array *(nekl-3^{+}; sur-5::GFP)*. An arrested larva is marked by the white arrow
630 and enlarged in the inset; the white bracket indicates the constricted region containing a
631 double cuticle. (B, C) DIC images of *nekl-2; nekl-3* double-mutant adult worms containing the
632 *adm-2(fd130)* (B) and *adm-2(fd163)* (C) mutant alleles. Bar size in A = 100 µm (for A–C); in inset,
633 20 µm. (D) Schematic diagram of the *adm-2* locus. Solid black rectangles indicate exons; introns
634 are demarcated by black lines. Locations of the *fd163*, *fd130*, *fd208*, and *fd243–fd247* alleles
635 are indicated by arrows. Large deletion alleles *fd298–fd302 fd313, fd316–fd318, fd228–fd230*,
636 and *fd235–fd237* are indicated by orange and blue lines. (E) Bar plot showing percentage of
637 viable adult-stage *nekl-2; nekl-3* worms with the indicated *adm-2* alleles (or RNAi); + indicates
638 wild-type *adm-2*. (F) Bar plot showing reversion of suppression in *nekl-2; nekl-3 adm-2(fd130)*
639 mutants by fosmids expressing wild-type *adm-2* and by an *adm-2* cDNA fused to GFP (pDF417).
640 Fosmid #1 and #2 indicate two independent extrachromosomal lines. (G) Bar plot showing
641 failure to suppress molting defects in *nekl–mlt* hypomorphic mutants by *adm-2* null mutants
642 [*nekl-2(fd91); adm-2(fd313)*, *nekl-3(sv3); adm-2(fd316)*, and *mlt-4(sv9); adm-2(fd317)*]. Error
643 bars in E–G represent 95% confidence intervals. p-Values were determined using Fisher's exact
644 test; ****$p \leq 0.0001$.

645

646 **Fig 2. Loss of *adm-2* function does not correct the *nekl* trafficking defects**

647 (A–C) Representative confocal images of 2-day-old adult worms expressing LRP-1::GFP in the
648 apical hyp7 region of the epidermis. LRP-1 expression in the *nekl-3::AID* (A), *nekl-3::AID*; *fcho-*
649 *1(ox477)* (B), and *nekl-3::AID; adm-2(fd318)* (C) mutant backgrounds in the absence (–) and
650 presence (+) of auxin treatment. Bar in A = 5 µm (for A–C). (D) Dot plot showing the percentage
651 of GFP-positive pixels within the apical plane of the worm epidermis for individuals of the
652 specified genotypes and auxin treatment groups. Group means along with 95% confidence
653 intervals (error bars) are indicated. p-Values were obtained by comparing means using an
654 unpaired t-test: ****$p \leq 0.0001$, *$p \leq 0.05$.

655

656 **Fig 3. Expression of ADM-2 in the epidermis and other tissues**

657 (A–D and A') Representative confocal images of ADM-2 expression in the *C. elegans* hyp7
658 region. ADM-2::mScarlet (A, B) and ADM-2::GFP (C, D) expression at apical (A, C) and medial (B,
659 D) planes. A' is the inset from panel A. Bar in B = 5 µm (for A–D); in inset A' = 5 µm. (E–G and E'–
660 G') Representative DIC (E–G) and confocal (E'–G') images of ADM-2 expression. ADM-
661 2::mScarlet in the hyp7 hypodermis; seam cells; sensory neurons; and ALM, DNC, and VNC
662 neurons (E, E') and in spermatheca (G, G'). ADM-2::GFP expression in the distal germline,
663 oocytes, and spermatheca (F, F'). Bar in E' = 50 µm (for E, E'); in G' = 10 µm (for G, G'); in F' = 50
664 µm (for F, F').

665

666 **Fig 4. ADM-2 localization to endocytic compartments is affected by NEKL activity**

667 (A–L) Co-localization analysis of ADM-2::mScarlet with GFP::CHC-1 (A–C), P_{hyp7}::HGRS-1::GFP
668 (D–F), and LysoTracker Green (G–L) within apical (A–C) and sub-apical or medial (D–L) planes of
669 hyp7. A'–F' are insets of A–F confocal images. White arrowheads in C' and F' indicate
670 colocalized puncta. For LysoTracker studies (G–L), representative confocal images during
671 intermolt (G–I) and molting (J–L) stages are shown. (M–P) Apical hyp7 ADM-2::mScarlet
672 localization in auxin-treated wild-type (M), *nekl-2::AID* (N), and *nekl-3::AID* (O) 2-day-old adults
673 with average mean intensity calculations (P). Group means along with 95% confidence intervals
674 (error bars) are indicated. p-Values were obtained by comparing means using an unpaired t-
675 test: ****$p \leq 0.0001$, **$p \leq 0.01$. Bar in M = 5 µm (for A–F and M–O); in F' = 5 µm (for insets A'–
676 F'); in L = 5 µm (for G–L).

677

678 **Fig 5. Functional analysis of ADM-2 domains**

679 (A) Schematic representation of predicted protein domains within ADM-2. PRO, prodomain;
680 MTP, metalloprotease domain; DIS, disintegrin domain; CYS-R, cysteine repeat region; TM,
681 transmembrane domain; NLS, predicted nuclear localization signal; DM, disintegrin motif; CysL,
682 cysteine loop; SH3 binding (1–3) Src homology 3 binding domains. (B) Color-coded peptide
683 sequence of ADM-2 corresponding to panel A. For additional details see S2 Fig. (C) Percentage

684 of viable (non-molting-defective) *nekl-2; nekl-3* adults in the indicated CRISPR-derived *adm-2*
685 mutant backgrounds. Error bars represent 95% confidence intervals. p-Values were determined
686 using Fisher's exact test: ****p ≤ 0.0001; ns, not significant. (D–F) Predicted three-dimensional
687 protein structures (for amino acid region 307–328) of wild-type ADM-2 (orange) superimposed
688 on modeled structures for the Furin-1 (D; red), DM (E; cyan), and CysL (F; violet) mutant
689 proteins. Three conserved histidine residues (His312, His316, His322) of the Zn-metalloprotease
690 domain are represented as sticks. (F) A predicted 6.1-Å shift of the 'tele' nitrogen atom in the
691 imidazole ring of His322 in the CysL mutant**.**
692
693 **Fig 6. ADM-2 is a negative regulator of molting and LRP-1**
694 (A) Bar plot showing the percentage of molting defects in the specified strains in the presence
695 and absence of the $P_{hsp\text{-}16}$*::adm-2::GFP* transgene in the wild-type background and in the
696 presence and absence of heat shock. Error bars represent 95% confidence intervals. p-Values
697 were determined using Fisher's exact test: ****p ≤ 0.0001. (B,C) Merged DIC and fluorescence
698 images of an adult worm carrying the $P_{hsp\text{-}16}$*::adm-2::GFP* transgene in the absence of heat
699 shock (B) and after heat shock (C). (D) Molting-defective larva after heat shock. White arrow in
700 D indicates unshed old cuticle. (E) Rare blister phenotype in a worm after ADM-2::GFP
701 induction. White arrowheads in E indicate blisters. Bar in C = 50 µm (for B and C); in D = 50 µm;
702 in E = 50 µm. (F,G) Representative confocal images of 1-day-old adult wild-type (F) and *adm-*
703 *2(fd300)* (G) worms expressing LRP-1::GFP in the hyp7 region of the hypodermis. Bar in F = 5 µm
704 (for F,G). (H) Dot plot showing LRP-1::GFP mean intensity (a.u.) within the apical plane of the
705 worm hypodermis for each individual worm of the specified genotype. (I–L) Representative
706 confocal images of 1-day-old adult worms expressing LRP-1::GFP in the hyp7 region of the
707 hypodermis. (I,J) LRP-1 expression in wild-type control worms. (K,L) LRP-1 expression in worms
708 containing the $P_{hsp\text{-}16}$*::adm-2* transgene. Worms are shown in the absence of heat shock (I,K)
709 and after heat shock (J,L). Bar in I = 10 µm (for I–L). (M) Dot plot showing LRP-1::GFP mean
710 intensity (a.u.) within the apical plane of the worm hypodermis for each individual worm of the
711 specified genotype and heat shock conditions. In H and M, group means along with 95%
712 confidence intervals (error bars) are indicated. p-Values were obtained by comparing means

713 using an unpaired t-test: ****p ≤ 0.0001; ***p ≤ 0.001; ns, p ≥ 0.05. (N) Genetic model of ADM-
714 2 function in *C. elegans* molting.
715
716 **S1 Fig. Loss of [other] *C. elegans* ADAM family members does not suppress *nekl* defects**
717 (A) Dot plot showing average brood sizes for 10 individual wild-type and *adm-2(fd300)* mutant
718 worms. (B) Bar plot showing the failure of most *C. elegans* ADAM family members to suppress
719 molting defects in *nekl-2; nekl-3* mutants. (C) Table showing ADM-2 *C. elegans* orthologs and
720 their corresponding human homologs. Error bars in A,B represent 95% confidence intervals. p-
721 Values were determined using an unpaired t-test (A) (ns, p ≥ 0.05) or Fisher's exact test (B):
722 ****p ≤ 0.0001.
723
724 **S2 Fig. Alignment of *C. elegans* ADM-2 with human ADAMs**
725 Peptide alignment of *C. elegans* ADM-2 with human meltrin family members
726 (ADAM9/12/19/33). Predicted domains of ADM-2 are color coded. NLS, nuclear localization
727 domain.
728
729 **S3 Fig. Additional ADM-2 expression**
730 (A–F and A'–F') Representative DIC (A–F) and confocal (A'–F') images of ADM-2 expression
731 showing the anterior hypodermis (A, A'), nerve ring (B, B'), tail neurons (C, C'), and various
732 stages of embryonic development (D–F'). Bar in A' = 10 µm (for A, A'); in B' = 10 µm (for B, B');
733 in C' = 10 µm (for C, C'); in F' = 10 µm (for D–F'). (G) Representative confocal image of an L2
734 larva expressing multi-copy $P_{adm\text{-}2}$::ADM-2::GFP in the plasma membrane of head neurons. Bar
735 in G = 25 µm.
736
737 **S4 Fig. Supplemental colocalization data**
738 (A,B) Dot plots showing quantification of Mander's overlap coefficient for the overlap of ADM-
739 2::mScarlet with GFP::CHC-1 and P_{hyp7}::HGRS-1::GFP proteins within the apical (A) and medial
740 (B) planes. Mean values and 95% confidence intervals (error bars) are indicated. p-Values were
741 calculated using an unpaired test: ****p ≤ 0.0001, **p ≤ 0.01. (C–H) Representative confocal

742 images of GFP::CHC-1 (C), P_{hyp7}::HGRS-1::GFP (F), and ADM-2::mScarlet (D,G) within the hyp7
743 medial plane. C'–H' are insets of C–H confocal images. Bar in E= 10 µm (for C–H); in E' = 5 µm
744 (for insets C'–H'). (E',H') White arrows show ADM-2 large vesicular structures that do not
745 colocalize with GFP::CHC-1 and P_{hyp7}HGRS-1::GFP puncta, which are lysosomes. Cyan arrows
746 indicate vesicles containing ADM-2 that colocalize with GFP::CHC-1 and P_{hyp7}::HGRS-1::GFP.
747
748 **S5 Fig. ADM-2 levels are increased slightly upon weak loss of *mlt-3***
749 (A,B) Dot plot showing the mean intensity (a.u.) of GFP::CHC-1 (A) and ADM-2::mScarlet (B)
750 expression in the presence of Control RNAi (i.e., empty vector) and *mlt-3* RNAi. Group means
751 along with 95% confidence intervals (error bars) are indicated. p-Values were obtained by
752 comparing means using an unpaired t-test: **$p \leq 0.01$, *$p \leq 0.05$.
753
754 **S6 Fig. Mutations in the C-terminal region of ADM-2 do not cause conformational changes to**
755 **the metalloprotease active site**
756 Three-dimensional protein structure of the region including amino acids 307–328 of wild-type
757 ADM-2 (orange) superimposed on modeled structures of SH3-1, SH3-2, and SH3-3 mutant
758 proteins.
759
760 **S7 Fig. Clathrin expression is not perturbed by loss of ADM-2 function**
761 (A,B) Representative confocal images of GFP::CHC-1 expression in the hyp7 region of the
762 hypodermis in the apical plane in wild-type (A) and *adm-2(fd300)* null mutant (B) 1-day-old
763 adult worms. Bar in A = 10 µm (for A,B). (C,D) Dot plots showing GFP::CHC-1 mean intensity
764 (a.u.) (C) and the percentage of GFP-positive pixels (D) within the apical plane for each
765 individual worm of the specified genotype. In C and D, group means along with 95% confidence
766 intervals (error bars) are indicated. p-Values were obtained by comparing means using an
767 unpaired t-test. ns, $p > 0.05$.
768
769 **S1 Table. List of all the strains used in this study (pdf).**
770 **S1 File. Compilation or raw data used in this study (MS Excel).**

771 **S2 File. List of primers used in this study (MS Excel).**

772

773 **References**

774 1. Page AP, Johnstone IL. The cuticle. WormBook. 2007:1-15. Epub 2007/12/01. doi:
775 10.1895/wormbook.1.138.1. PubMed PMID: 18050497.
776 2. Lazetic V, Fay DS. Molting in C. elegans. Worm. 2017;6(1):e1330246. Epub 2017/07/14.
777 doi: 10.1080/21624054.2017.1330246. PubMed PMID: 28702275; PubMed Central PMCID:
778 PMCPMC5501215.
779 3. Antebi A. Nuclear hormone receptors in C. elegans. WormBook. 2006:1-13. Epub
780 2007/12/01. doi: 10.1895/wormbook.1.64.1. PubMed PMID: 18050471; PubMed Central
781 PMCID: PMCPMC4781232.
782 4. Gissendanner CR, Crossgrove K, Kraus KA, Maina CV, Sluder AE. Expression and function
783 of conserved nuclear receptor genes in Caenorhabditis elegans. Dev Biol. 2004;266(2):399-416.
784 Epub 2004/01/24. doi: 10.1016/j.ydbio.2003.10.014. PubMed PMID: 14738886.
785 5. Kang YL, Yochem J, Bell L, Sorensen EB, Chen L, Conner SD. Caenorhabditis elegans
786 reveals a FxNPxY-independent low-density lipoprotein receptor internalization mechanism
787 mediated by epsin1. Mol Biol Cell. 2013;24(3):308-18. Epub 2012/12/18. doi: mbc.E12-02-0163
788 [pii]
789 10.1091/mbc.E12-02-0163. PubMed PMID: 23242996; PubMed Central PMCID: PMC3564534.
790 6. Yochem J, Tuck S, Greenwald I, Han M. A gp330/megalin-related protein is required in
791 the major epidermis of Caenorhabditis elegans for completion of molting. Development.
792 1999;126(3):597-606. Epub 1999/01/07. PubMed PMID: 9876188.
793 7. Roudier N, Lefebvre C, Legouis R. CeVPS-27 is an endosomal protein required for the
794 molting and the endocytic trafficking of the low-density lipoprotein receptor-related protein 1
795 in Caenorhabditis elegans. Traffic. 2005;6(8):695-705. Epub 2005/07/07. doi: 10.1111/j.1600-
796 0854.2005.00309.x. PubMed PMID: 15998324.
797 8. Yochem J, Lazetic V, Bell L, Chen L, Fay D. C. elegans NIMA-related kinases NEKL-2 and
798 NEKL-3 are required for the completion of molting. Dev Biol. 2015;398(2):255-66. Epub
799 2014/12/20. doi: S0012-1606(14)00634-4 [pii]
800 10.1016/j.ydbio.2014.12.008. PubMed PMID: 25523392; PubMed Central PMCID: PMC4314388.
801 9. Lazetic V, Fay DS. Conserved ankyrin repeat proteins and their NIMA kinase partners
802 regulate extracellular matrix remodeling and intracellular trafficking in Caenorhabditis elegans.
803 Genetics. 2017;205:273-93.
804 10. Lazetic V, Joseph BB, Bernazzani SM, Fay DS. Actin organization and endocytic trafficking
805 are controlled by a network linking NIMA-related kinases to the CDC-42-SID-3/ACK1 pathway.
806 PLoS Genet. 2018;14(4):e1007313. Epub 2018/04/03. doi: 10.1371/journal.pgen.1007313.
807 PubMed PMID: 29608564; PubMed Central PMCID: PMCPMC5897031.
808 11. Joseph BB, Wang Y, Edeen P, Lazetic V, Grant BD, Fay DS. Control of clathrin-mediated
809 endocytosis by NIMA family kinases. PLoS Genet. 2020;16(2):e1008633. Epub 2020/02/19. doi:
810 10.1371/journal.pgen.1008633. PubMed PMID: 32069276.

811 12. Binti S.: Melinda RVJ, B.B.; Edeen, P., Miller, S.D.; Fay, D.S. A life cycle alteration can
812 correct molting defects in Caenorhabditis elegans. bioRxiv.
813 2021;https://doi.org/10.1101/2021.11.02.466921. Epub November 4, 2021.
814 13. Oakley BR, Morris NR. A mutation in Aspergillus nidulans that blocks the transition from
815 interphase to prophase. J Cell Biol. 1983;96(4):1155-8. Epub 1983/04/01. doi:
816 10.1083/jcb.96.4.1155. PubMed PMID: 6339527; PubMed Central PMCID: PMCPMC2112314.
817 14. Osmani SA, May GS, Morris NR. Regulation of the mRNA levels of nimA, a gene required
818 for the G2-M transition in Aspergillus nidulans. J Cell Biol. 1987;104(6):1495-504. Epub
819 1987/06/01. doi: 10.1083/jcb.104.6.1495. PubMed PMID: 3294854; PubMed Central PMCID:
820 PMCPMC2114495.
821 15. Casey JP, Brennan K, Scheidel N, McGettigan P, Lavin PT, Carter S, et al. Recessive NEK9
822 mutation causes a lethal skeletal dysplasia with evidence of cell cycle and ciliary defects. Hum
823 Mol Genet. 2016;25(9):1824-35. Epub 2016/02/26. doi: 10.1093/hmg/ddw054. PubMed PMID:
824 26908619.
825 16. Fry AM, O'Regan L, Sabir SR, Bayliss R. Cell cycle regulation by the NEK family of protein
826 kinases. J Cell Sci. 2012;125(Pt 19):4423-33. Epub 2012/11/08. doi: jcs.111195 [pii]
827 10.1242/jcs.111195. PubMed PMID: 23132929; PubMed Central PMCID: PMC3500863.
828 17. Moniz L, Dutt P, Haider N, Stambolic V. Nek family of kinases in cell cycle, checkpoint
829 control and cancer. Cell Div. 2011;6:18. Epub 2011/11/02. doi: 1747-1028-6-18 [pii]
830 10.1186/1747-1028-6-18. PubMed PMID: 22040655; PubMed Central PMCID: PMC3222597.
831 18. Osmani AH, McGuire SL, Osmani SA. Parallel activation of the NIMA and p34cdc2 cell
832 cycle-regulated protein kinases is required to initiate mitosis in A. nidulans. Cell.
833 1991;67(2):283-91. Epub 1991/10/18. doi: 10.1016/0092-8674(91)90180-7. PubMed PMID:
834 1913824.
835 19. Manning DK, Sergeev M, van Heesbeen RG, Wong MD, Oh JH, Liu Y, et al. Loss of the
836 ciliary kinase Nek8 causes left-right asymmetry defects. J Am Soc Nephrol. 2013;24(1):100-12.
837 Epub 2013/01/01. doi: 10.1681/ASN.2012050490. PubMed PMID: 23274954; PubMed Central
838 PMCID: PMCPMC3537214.
839 20. Quarmby LM, Mahjoub MR. Caught Nek-ing: cilia and centrioles. J Cell Sci. 2005;118(Pt
840 22):5161-9. Epub 2005/11/11. doi: 118/22/5161 [pii]
841 10.1242/jcs.02681. PubMed PMID: 16280549.
842 21. Trapp ML, Galtseva A, Manning DK, Beier DR, Rosenblum ND, Quarmby LM. Defects in
843 ciliary localization of Nek8 is associated with cystogenesis. Pediatr Nephrol. 2008;23(3):377-87.
844 Epub 2008/01/15. doi: 10.1007/s00467-007-0692-y. PubMed PMID: 18189147.
845 22. Otto EA, Trapp ML, Schultheiss UT, Helou J, Quarmby LM, Hildebrandt F. NEK8
846 mutations affect ciliary and centrosomal localization and may cause nephronophthisis. J Am Soc
847 Nephrol. 2008;19(3):587-92. Epub 2008/01/18. doi: ASN.2007040490 [pii]
848 10.1681/ASN.2007040490. PubMed PMID: 18199800; PubMed Central PMCID: PMC2391043.
849 23. Walker C, Mojares E, Del Rio Hernandez A. Role of Extracellular Matrix in Development
850 and Cancer Progression. Int J Mol Sci. 2018;19(10). Epub 2018/10/06. doi:
851 10.3390/ijms19103028. PubMed PMID: 30287763; PubMed Central PMCID: PMCPMC6213383.
852 24. Wang R, Song Y, Xu X, Wu Q, Liu C. The expression of Nek7, FoxM1, and Plk1 in
853 gallbladder cancer and their relationships to clinicopathologic features and survival. Clin Transl

854 Oncol. 2013;15(8):626-32. Epub 2013/01/30. doi: 10.1007/s12094-012-0978-9. PubMed PMID:
855 23359173.
856 25. Choudhury AD, Schinzel AC, Cotter MB, Lis RT, Labella K, Lock YJ, et al. Castration
857 Resistance in Prostate Cancer Is Mediated by the Kinase NEK6. Cancer Res. 2017;77(3):753-65.
858 Epub 2016/12/03. doi: 10.1158/0008-5472.CAN-16-0455. PubMed PMID: 27899381; PubMed
859 Central PMCID: PMCPMC5290202.
860 26. He Z, Ni X, Xia L, Shao Z. Overexpression of NIMA-related kinase 6 (NEK6) contributes to
861 malignant growth and dismal prognosis in Human Breast Cancer. Pathol Res Pract.
862 2018;214(10):1648-54. Epub 2018/08/30. doi: 10.1016/j.prp.2018.07.030. PubMed PMID:
863 30153958.
864 27. Jee HJ, Kim AJ, Song N, Kim HJ, Kim M, Koh H, et al. Nek6 overexpression antagonizes
865 p53-induced senescence in human cancer cells. Cell Cycle. 2010;9(23):4703-10. Epub
866 2010/11/26. doi: 14059 [pii]. PubMed PMID: 21099361.
867 28. Jee HJ, Kim HJ, Kim AJ, Song N, Kim M, Lee HJ, et al. The inhibition of Nek6 function
868 sensitizes human cancer cells to premature senescence upon serum reduction or anticancer
869 drug treatment. Cancer Lett. 2013;335(1):175-82. Epub 2013/02/19. doi: S0304-3835(13)00124-
870 9 [pii]
871 10.1016/j.canlet.2013.02.012. PubMed PMID: 23416273.
872 29. Joseph BB, Blouin NA, Fay DS. Use of a Sibling Subtraction Method for Identifying Causal
873 Mutations in Caenorhabditis elegans by Whole-Genome Sequencing. G3 (Bethesda, Md).
874 2018;8(2):669-78. Epub 2017/12/15. doi: 10.1534/g3.117.300135. PubMed PMID: 29237702;
875 PubMed Central PMCID: PMCPMC5919755.
876 30. Seals DF, Courtneidge SA. The ADAMs family of metalloproteases: multidomain proteins
877 with multiple functions. Genes Dev. 2003;17(1):7-30. Epub 2003/01/07. doi:
878 10.1101/gad.1039703. PubMed PMID: 12514095.
879 31. Giebeler N, Zigrino P. A Disintegrin and Metalloprotease (ADAM): Historical Overview of
880 Their Functions. Toxins (Basel). 2016;8(4):122. Epub 2016/04/28. doi: 10.3390/toxins8040122.
881 PubMed PMID: 27120619; PubMed Central PMCID: PMCPMC4848645.
882 32. Alfandari D, McCusker C, Cousin H. ADAM function in embryogenesis. Semin Cell Dev
883 Biol. 2009;20(2):153-63. Epub 2008/10/22. doi: 10.1016/j.semcdb.2008.09.006. PubMed PMID:
884 18935966; PubMed Central PMCID: PMCPMC2693894.
885 33. Cousin H, Abbruzzese G, Kerdavid E, Gaultier A, Alfandari D. Translocation of the
886 cytoplasmic domain of ADAM13 to the nucleus is essential for Calpain8-a expression and cranial
887 neural crest cell migration. Dev Cell. 2011;20(2):256-63. Epub 2011/02/15. doi:
888 10.1016/j.devcel.2010.12.009. PubMed PMID: 21316592; PubMed Central PMCID:
889 PMCPMC3074609.
890 34. Brocker CN, Vasiliou V, Nebert DW. Evolutionary divergence and functions of the ADAM
891 and ADAMTS gene families. Hum Genomics. 2009;4(1):43-55. Epub 2009/12/03. doi:
892 10.1186/1479-7364-4-1-43. PubMed PMID: 19951893; PubMed Central PMCID:
893 PMCPMC3500187.
894 35. Yagami-Hiromasa T, Sato T, Kurisaki T, Kamijo K, Nabeshima Y, Fujisawa-Sehara A. A
895 metalloprotease-disintegrin participating in myoblast fusion. Nature. 1995;377(6550):652-6.
896 Epub 1995/10/19. doi: 10.1038/377652a0. PubMed PMID: 7566181.

897 36. Weskamp G, Cai H, Brodie TA, Higashyama S, Manova K, Ludwig T, et al. Mice lacking the
898 metalloprotease-disintegrin MDC9 (ADAM9) have no evident major abnormalities during
899 development or adult life. Mol Cell Biol. 2002;22(5):1537-44. Epub 2002/02/13. doi:
900 10.1128/mcb.22.5.1537-1544.2002. PubMed PMID: 11839819; PubMed Central PMCID:
901 PMCPMC134708.
902 37. Sahin U, Weskamp G, Kelly K, Zhou HM, Higashiyama S, Peschon J, et al. Distinct roles
903 for ADAM10 and ADAM17 in ectodomain shedding of six EGFR ligands. J Cell Biol.
904 2004;164(5):769-79. Epub 2004/03/03. doi: 10.1083/jcb.200307137. PubMed PMID: 14993236;
905 PubMed Central PMCID: PMCPMC2172154.
906 38. Primakoff P, Myles DG. The ADAM gene family: surface proteins with adhesion and
907 protease activity. Trends Genet. 2000;16(2):83-7. Epub 2000/02/01. doi: 10.1016/s0168-
908 9525(99)01926-5. PubMed PMID: 10652535.
909 39. Mygind KJ, Storiko T, Freiberg ML, Samsoe-Petersen J, Schwarz J, Andersen OM, et al.
910 Sorting nexin 9 (SNX9) regulates levels of the transmembrane ADAM9 at the cell surface. J Biol
911 Chem. 2018;293(21):8077-88. Epub 2018/04/07. doi: 10.1074/jbc.RA117.001077. PubMed
912 PMID: 29622675; PubMed Central PMCID: PMCPMC5971451.
913 40. Stautz D, Leyme A, Grandal MV, Albrechtsen R, van Deurs B, Wewer U, et al. Cell-surface
914 metalloprotease ADAM12 is internalized by a clathrin- and Grb2-dependent mechanism. Traffic.
915 2012;13(11):1532-46. Epub 2012/08/14. doi: 10.1111/j.1600-0854.2012.01405.x. PubMed
916 PMID: 22882974.
917 41. Lorenzen I, Lokau J, Korpys Y, Oldefest M, Flynn CM, Kunzel U, et al. Control of ADAM17
918 activity by regulation of its cellular localisation. Sci Rep. 2016;6:35067. Epub 2016/10/13. doi:
919 10.1038/srep35067. PubMed PMID: 27731361; PubMed Central PMCID: PMCPMC5059621.
920 42. Marcello E, Saraceno C, Musardo S, Vara H, de la Fuente AG, Pelucchi S, et al.
921 Endocytosis of synaptic ADAM10 in neuronal plasticity and Alzheimer's disease. J Clin Invest.
922 2013;123(6):2523-38. Epub 2013/05/17. doi: 10.1172/JCI65401. PubMed PMID: 23676497;
923 PubMed Central PMCID: PMCPMC3668814.
924 43. Kim DW, Sung H, Shin D, Shen H, Ahnn J, Lee SK, et al. Differential physiological roles of
925 ESCRT complexes in Caenorhabditis elegans. Mol Cells. 2011;31(6):585-92. Epub 2011/06/21.
926 doi: 10.1007/s10059-011-1045-z. PubMed PMID: 21688204; PubMed Central PMCID:
927 PMCPMC3887624.
928 44. Hurley JH. The ESCRT complexes. Crit Rev Biochem Mol Biol. 2010;45(6):463-87. Epub
929 2010/07/27. doi: 10.3109/10409238.2010.502516. PubMed PMID: 20653365; PubMed Central
930 PMCID: PMCPMC2988974.
931 45. Henne WM, Buchkovich NJ, Emr SD. The ESCRT pathway. Dev Cell. 2011;21(1):77-91.
932 Epub 2011/07/19. doi: 10.1016/j.devcel.2011.05.015. PubMed PMID: 21763610.
933 46. Babst M. MVB vesicle formation: ESCRT-dependent, ESCRT-independent and everything
934 in between. Curr Opin Cell Biol. 2011;23(4):452-7. Epub 2011/05/17. doi:
935 10.1016/j.ceb.2011.04.008. PubMed PMID: 21570275; PubMed Central PMCID:
936 PMCPMC3148405.
937 47. Miao R, Li M, Zhang Q, Yang C, Wang X. An ECM-to-Nucleus Signaling Pathway Activates
938 Lysosomes for C. elegans Larval Development. Dev Cell. 2020;52(1):21-37 e5. Epub 2019/11/19.
939 doi: 10.1016/j.devcel.2019.10.020. PubMed PMID: 31735670.

940 48. Kneen M, Farinas J, Li Y, Verkman AS. Green fluorescent protein as a noninvasive
941 intracellular pH indicator. Biophys J. 1998;74(3):1591-9. Epub 1998/03/25. doi: 10.1016/S0006-
942 3495(98)77870-1. PubMed PMID: 9512054; PubMed Central PMCID: PMCPMC1299504.
943 49. Bode W, Gomis-Ruth FX, Stockler W. Astacins, serralysins, snake venom and matrix
944 metalloproteinases exhibit identical zinc-binding environments (HEXXHXXGXXH and Met-turn)
945 and topologies and should be grouped into a common family, the 'metzincins'. FEBS Lett.
946 1993;331(1-2):134-40. Epub 1993/09/27. doi: 10.1016/0014-5793(93)80312-i. PubMed PMID:
947 8405391.
948 50. Maskos K, Fernandez-Catalan C, Huber R, Bourenkov GP, Bartunik H, Ellestad GA, et al.
949 Crystal structure of the catalytic domain of human tumor necrosis factor-alpha-converting
950 enzyme. Proc Natl Acad Sci U S A. 1998;95(7):3408-12. Epub 1998/05/09. doi:
951 10.1073/pnas.95.7.3408. PubMed PMID: 9520379; PubMed Central PMCID: PMCPMC19849.
952 51. Jumper J, Evans R, Pritzel A, Green T, Figurnov M, Ronneberger O, et al. Highly accurate
953 protein structure prediction with AlphaFold. Nature. 2021;596(7873):583-9. Epub 2021/07/16.
954 doi: 10.1038/s41586-021-03819-2. PubMed PMID: 34265844; PubMed Central PMCID:
955 PMCPMC8371605.
956 52. Varadi M, Anyango S, Deshpande M, Nair S, Natassia C, Yordanova G, et al. AlphaFold
957 Protein Structure Database: massively expanding the structural coverage of protein-sequence
958 space with high-accuracy models. Nucleic Acids Res. 2021. Epub 2021/11/19. doi:
959 10.1093/nar/gkab1061. PubMed PMID: 34791371.
960 53. Song Y, DiMaio F, Wang RY, Kim D, Miles C, Brunette T, et al. High-resolution
961 comparative modeling with RosettaCM. Structure. 2013;21(10):1735-42. Epub 2013/09/17. doi:
962 10.1016/j.str.2013.08.005. PubMed PMID: 24035711; PubMed Central PMCID:
963 PMCPMC3811137.
964 54. Raman S, Vernon R, Thompson J, Tyka M, Sadreyev R, Pei J, et al. Structure prediction
965 for CASP8 with all-atom refinement using Rosetta. Proteins. 2009;77 Suppl 9:89-99. Epub
966 2009/08/25. doi: 10.1002/prot.22540. PubMed PMID: 19701941; PubMed Central PMCID:
967 PMCPMC3688471.
968 55. Glassey B, Civetta A. Positive selection at reproductive ADAM genes with potential
969 intercellular binding activity. Mol Biol Evol. 2004;21(5):851-9. Epub 2004/02/14. doi:
970 10.1093/molbev/msh080. PubMed PMID: 14963094.
971 56. Black RA, Rauch CT, Kozlosky CJ, Peschon JJ, Slack JL, Wolfson MF, et al. A
972 metalloproteinase disintegrin that releases tumour-necrosis factor-alpha from cells. Nature.
973 1997;385(6618):729-33. Epub 1997/02/20. doi: 10.1038/385729a0. PubMed PMID: 9034190.
974 57. Moss ML, Jin SL, Milla ME, Bickett DM, Burkhart W, Carter HL, et al. Cloning of a
975 disintegrin metalloproteinase that processes precursor tumour-necrosis factor-alpha. Nature.
976 1997;385(6618):733-6. Epub 1997/02/20. doi: 10.1038/385733a0. PubMed PMID: 9034191.
977 58. Lunn CA, Fan X, Dalie B, Miller K, Zavodny PJ, Narula SK, et al. Purification of ADAM 10
978 from bovine spleen as a TNFalpha convertase. FEBS Lett. 1997;400(3):333-5. Epub 1997/01/06.
979 doi: 10.1016/s0014-5793(96)01410-x. PubMed PMID: 9009225.
980 59. Rosendahl MS, Ko SC, Long DL, Brewer MT, Rosenzweig B, Hedl E, et al. Identification
981 and characterization of a pro-tumor necrosis factor-alpha-processing enzyme from the ADAM
982 family of zinc metalloproteases. J Biol Chem. 1997;272(39):24588-93. Epub 1997/09/26. doi:
983 10.1074/jbc.272.39.24588. PubMed PMID: 9305925.

984 60. Reddy P, Slack JL, Davis R, Cerretti DP, Kozlosky CJ, Blanton RA, et al. Functional analysis
985 of the domain structure of tumor necrosis factor-alpha converting enzyme. J Biol Chem.
986 2000;275(19):14608-14. Epub 2000/05/09. doi: 10.1074/jbc.275.19.14608. PubMed PMID:
987 10799547.
988 61. Solomon KA, Pesti N, Wu G, Newton RC. Cutting edge: a dominant negative form of TNF-
989 alpha converting enzyme inhibits proTNF and TNFRII secretion. J Immunol. 1999;163(8):4105-8.
990 Epub 1999/10/08. PubMed PMID: 10510344.
991 62. Zhang Z, Oliver P, Lancaster JR, Jr., Schwarzenberger PO, Joshi MS, Cork J, et al. Reactive
992 oxygen species mediate tumor necrosis factor alpha-converting, enzyme-dependent
993 ectodomain shedding induced by phorbol myristate acetate. FASEB J. 2001;15(2):303-5. Epub
994 2001/02/07. doi: 10.1096/fj.00-0371fje. PubMed PMID: 11156944.
995 63. Althoff K, Reddy P, Voltz N, Rose-John S, Mullberg J. Shedding of interleukin-6 receptor
996 and tumor necrosis factor alpha. Contribution of the stalk sequence to the cleavage pattern of
997 transmembrane proteins. Eur J Biochem. 2000;267(9):2624-31. Epub 2000/04/28. doi:
998 10.1046/j.1432-1327.2000.01278.x. PubMed PMID: 10785383.
999 64. Fischer OM, Hart S, Gschwind A, Ullrich A. EGFR signal transactivation in cancer cells.
1000 Biochem Soc Trans. 2003;31(Pt 6):1203-8. Epub 2003/12/04. doi: 10.1042/bst0311203. PubMed
1001 PMID: 14641026.
1002 65. Prenzel N, Zwick E, Daub H, Leserer M, Abraham R, Wallasch C, et al. EGF receptor
1003 transactivation by G-protein-coupled receptors requires metalloproteinase cleavage of proHB-
1004 EGF. Nature. 1999;402(6764):884-8. Epub 2000/01/06. doi: 10.1038/47260. PubMed PMID:
1005 10622253.
1006 66. Yan Y, Shirakabe K, Werb Z. The metalloprotease Kuzbanian (ADAM10) mediates the
1007 transactivation of EGF receptor by G protein-coupled receptors. J Cell Biol. 2002;158(2):221-6.
1008 Epub 2002/07/18. doi: 10.1083/jcb.200112026. PubMed PMID: 12119356; PubMed Central
1009 PMCID: PMCPMC2173139.
1010 67. Lemjabbar H, Basbaum C. Platelet-activating factor receptor and ADAM10 mediate
1011 responses to Staphylococcus aureus in epithelial cells. Nat Med. 2002;8(1):41-6. Epub
1012 2002/01/12. doi: 10.1038/nm0102-41. PubMed PMID: 11786905.
1013 68. Ohtsu H, Dempsey PJ, Eguchi S. ADAMs as mediators of EGF receptor transactivation by
1014 G protein-coupled receptors. Am J Physiol Cell Physiol. 2006;291(1):C1-10. Epub 2006/06/14.
1015 doi: 10.1152/ajpcell.00620.2005. PubMed PMID: 16769815.
1016 69. Kataoka H. EGFR ligands and their signaling scissors, ADAMs, as new molecular targets
1017 for anticancer treatments. J Dermatol Sci. 2009;56(3):148-53. Epub 2009/11/10. doi:
1018 10.1016/j.jdermsci.2009.10.002. PubMed PMID: 19896805.
1019 70. Brou C, Logeat F, Gupta N, Bessia C, LeBail O, Doedens JR, et al. A novel proteolytic
1020 cleavage involved in Notch signaling: the role of the disintegrin-metalloprotease TACE. Mol Cell.
1021 2000;5(2):207-16. Epub 2000/07/06. doi: 10.1016/s1097-2765(00)80417-7. PubMed PMID:
1022 10882063.
1023 71. Selvais C, Gaide Chevronnay HP, Lemoine P, Dedieu S, Henriet P, Courtoy PJ, et al.
1024 Metalloproteinase-dependent shedding of low-density lipoprotein receptor-related protein-1
1025 ectodomain decreases endocytic clearance of endometrial matrix metalloproteinase-2 and -9 at
1026 menstruation. Endocrinology. 2009;150(8):3792-9. Epub 2009/05/02. doi: 10.1210/en.2009-
1027 0015. PubMed PMID: 19406945.

1028 72. Liu Q, Zhang J, Tran H, Verbeek MM, Reiss K, Estus S, et al. LRP1 shedding in human
1029 brain: roles of ADAM10 and ADAM17. Mol Neurodegener. 2009;4:17. Epub 2009/04/18. doi:
1030 10.1186/1750-1326-4-17. PubMed PMID: 19371428; PubMed Central PMCID:
1031 PMCPMC2672942.
1032 73. Selvais C, D'Auria L, Tyteca D, Perrot G, Lemoine P, Troeberg L, et al. Cell cholesterol
1033 modulates metalloproteinase-dependent shedding of low-density lipoprotein receptor-related
1034 protein-1 (LRP-1) and clearance function. FASEB J. 2011;25(8):2770-81. Epub 2011/04/27. doi:
1035 10.1096/fj.10-169508. PubMed PMID: 21518850; PubMed Central PMCID: PMCPMC3470721.
1036 74. Emonard H, Theret L, Bennasroune AH, Dedieu S. Regulation of LRP-1 expression: make
1037 the point. Pathol Biol (Paris). 2014;62(2):84-90. Epub 2014/03/26. doi:
1038 10.1016/j.patbio.2014.02.002. PubMed PMID: 24661974.
1039 75. Dekky B, Wahart A, Sartelet H, Fere M, Angiboust JF, Dedieu S, et al. Cellular Cholesterol
1040 Distribution Influences Proteolytic Release of the LRP-1 Ectodomain. Front Pharmacol.
1041 2016;7:25. Epub 2016/02/24. doi: 10.3389/fphar.2016.00025. PubMed PMID: 26903870;
1042 PubMed Central PMCID: PMCPMC4751253.
1043 76. Calligaris M, Cuffaro D, Bonelli S, Spano DP, Rossello A, Nuti E, et al. Strategies to Target
1044 ADAM17 in Disease: From its Discovery to the iRhom Revolution. Molecules. 2021;26(4). Epub
1045 2021/02/14. doi: 10.3390/molecules26040944. PubMed PMID: 33579029; PubMed Central
1046 PMCID: PMCPMC7916773.
1047 77. Biemesderfer D. Regulated intramembrane proteolysis of megalin: linking urinary
1048 protein and gene regulation in proximal tubule? Kidney Int. 2006;69(10):1717-21. Epub
1049 2006/03/25. doi: 10.1038/sj.ki.5000298. PubMed PMID: 16557231.
1050 78. Zou Z, Chung B, Nguyen T, Mentone S, Thomson B, Biemesderfer D. Linking receptor-
1051 mediated endocytosis and cell signaling: evidence for regulated intramembrane proteolysis of
1052 megalin in proximal tubule. J Biol Chem. 2004;279(33):34302-10. Epub 2004/06/08. doi:
1053 10.1074/jbc.M405608200. PubMed PMID: 15180987.
1054 79. May P, Reddy YK, Herz J. Proteolytic processing of low density lipoprotein receptor-
1055 related protein mediates regulated release of its intracellular domain. J Biol Chem.
1056 2002;277(21):18736-43. Epub 2002/03/22. doi: 10.1074/jbc.M201979200. PubMed PMID:
1057 11907044.
1058 80. Spuch C, Ortolano S, Navarro C. LRP-1 and LRP-2 receptors function in the membrane
1059 neuron. Trafficking mechanisms and proteolytic processing in Alzheimer's disease. Front
1060 Physiol. 2012;3:269. Epub 2012/08/31. doi: 10.3389/fphys.2012.00269. PubMed PMID:
1061 22934024; PubMed Central PMCID: PMCPMC3429044.
1062 81. Quinn KA, Pye VJ, Dai YP, Chesterman CN, Owensby DA. Characterization of the soluble
1063 form of the low density lipoprotein receptor-related protein (LRP). Exp Cell Res.
1064 1999;251(2):433-41. Epub 1999/09/02. doi: 10.1006/excr.1999.4590. PubMed PMID:
1065 10471328.
1066 82. Stepek G, McCormack G, Birnie AJ, Page AP. The astacin metalloprotease moulting
1067 enzyme NAS-36 is required for normal cuticle ecdysis in free-living and parasitic nematodes.
1068 Parasitology. 2011;138(2):237-48. Epub 2010/08/31. doi: 10.1017/S0031182010001113.
1069 PubMed PMID: 20800010.
1070 83. Frand AR, Russel S, Ruvkun G. Functional genomic analysis of C. elegans molting. PLoS
1071 Biol. 2005;3(10):e312. Epub 2005/08/27. doi: 05-PLBI-RA-0162R2 [pii]

1072 10.1371/journal.pbio.0030312. PubMed PMID: 16122351; PubMed Central PMCID:
1073 PMC1233573.
1074 84. Suzuki M, Sagoh N, Iwasaki H, Inoue H, Takahashi K. Metalloproteases with EGF, CUB,
1075 and thrombospondin-1 domains function in molting of Caenorhabditis elegans. Biol Chem.
1076 2004;385(6):565-8. Epub 2004/07/17. doi: 10.1515/BC.2004.069. PubMed PMID: 15255192.
1077 85. Davis MW, Birnie AJ, Chan AC, Page AP, Jorgensen EM. A conserved metalloprotease
1078 mediates ecdysis in Caenorhabditis elegans. Development. 2004;131(23):6001-8. Epub
1079 2004/11/13. doi: 10.1242/dev.01454. PubMed PMID: 15539494.
1080 86. Hashmi S, Zhang J, Oksov Y, Lustigman S. The Caenorhabditis elegans cathepsin Z-like
1081 cysteine protease, Ce-CPZ-1, has a multifunctional role during the worms' development. J Biol
1082 Chem. 2004;279(7):6035-45. Epub 2003/11/25. doi: 10.1074/jbc.M312346200. PubMed PMID:
1083 14630920.
1084 87. Kim TH, Kim YJ, Cho JW, Shim J. A novel zinc-carboxypeptidase SURO-1 regulates cuticle
1085 formation and body morphogenesis in Caenorhabditis elegans. FEBS Lett. 2011;585(1):121-7.
1086 Epub 2010/11/26. doi: 10.1016/j.febslet.2010.11.020. PubMed PMID: 21094156.
1087 88. Stepek G, McCormack G, Page AP. The kunitz domain protein BLI-5 plays a functionally
1088 conserved role in cuticle formation in a diverse range of nematodes. Mol Biochem Parasitol.
1089 2010;169(1):1-11. Epub 2009/09/01. doi: 10.1016/j.molbiopara.2009.08.005. PubMed PMID:
1090 19716386.
1091 89. Page AP, McCormack G, Birnie AJ. Biosynthesis and enzymology of the Caenorhabditis
1092 elegans cuticle: identification and characterization of a novel serine protease inhibitor. Int J
1093 Parasitol. 2006;36(6):681-9. Epub 2006/02/28. doi: 10.1016/j.ijpara.2006.01.004. PubMed
1094 PMID: 16500660.
1095 90. Hendriks GJ, Gaidatzis D, Aeschimann F, Grosshans H. Extensive oscillatory gene
1096 expression during C. elegans larval development. Mol Cell. 2014;53(3):380-92. Epub
1097 2014/01/21. doi: 10.1016/j.molcel.2013.12.013. PubMed PMID: 24440504.
1098 91. Meeuse MW, Hauser YP, Morales Moya LJ, Hendriks GJ, Eglinger J, Bogaarts G, et al.
1099 Developmental function and state transitions of a gene expression oscillator in Caenorhabditis
1100 elegans. Mol Syst Biol. 2020;16(7):e9498. Epub 2020/07/21. doi: 10.15252/msb.20209498.
1101 PubMed PMID: 32687264; PubMed Central PMCID: PMCPMC7370751.
1102 92. Roberts B, Clucas C, Johnstone IL. Loss of SEC-23 in Caenorhabditis elegans causes
1103 defects in oogenesis, morphogenesis, and extracellular matrix secretion. Mol Biol Cell.
1104 2003;14(11):4414-26. Epub 2003/10/11. doi: 10.1091/mbc.e03-03-0162. PubMed PMID:
1105 14551256; PubMed Central PMCID: PMCPMC266761.
1106 93. Stiernagle T. Maintenance of C. elegans. WormBook. 2006:1-11. Epub 2007/12/01. doi:
1107 10.1895/wormbook.1.101.1. PubMed PMID: 18050451; PubMed Central PMCID:
1108 PMCPMC4781397.
1109 94. Fire A, Xu S, Montgomery MK, Kostas SA, Driver SE, Mello CC. Potent and specific
1110 genetic interference by double-stranded RNA in Caenorhabditis elegans. Nature.
1111 1998;391(6669):806-11. Epub 1998/03/05. doi: 10.1038/35888. PubMed PMID: 9486653.
1112 95. Ahringer J. Reverse Genetics, WormBook. 2005.
1113 96. Wang D, Kennedy S, Conte D, Jr., Kim JK, Gabel HW, Kamath RS, et al. Somatic
1114 misexpression of germline P granules and enhanced RNA interference in retinoblastoma

1115 pathway mutants. Nature. 2005;436(7050):593-7. Epub 2005/07/29. doi: 10.1038/nature04010.
1116 PubMed PMID: 16049496.
1117 97. Fay SF, Fay DS, Chhatre VE. CRISPRcruncher: A tool for engineering restriction sites into
1118 coding regions. MicroPubl Biol. 2021;2021. Epub 20210118. doi:
1119 10.17912/micropub.biology.000343. PubMed PMID: 33490886; PubMed Central PMCID:
1120 PMCPMC7816087.
1121 98. Fay DS, Gerow K. A biologist's guide to statistical thinking and analysis. WormBook.
1122 2013:1-54. Epub 2013/08/03. doi: 10.1895/wormbook.1.159.1. PubMed PMID: 23908055;
1123 PubMed Central PMCID: PMC3880567.
1124